Experimental Thermal and Fluid Science 132 (2022) 110573

Contents lists available at ScienceDirect

Experimental Thermal and Fluid Science

journal homepage: www.elsevier.com/locate/etfs

# An experimental study on mitigating dynamic ice accretion process on bridge cables with a superhydrophobic coating

Yihua Peng [a,b], Ramsankar Veerakumar [b], Zichen Zhang [b], Haiyang Hu [b], Yang Liu [b], Xuhui He [a,c,d], Hui Hu [b,*]

[a] School of Civil Engineering, Central South University, Changsha 410075, China
[b] Department of Aerospace Engineering, Iowa State University, Ames, IA 50011-1096, United States
[c] National Engineering Laboratory for High-Speed Railway Construction, Changsha 410075, China
[d] Joint International Research Laboratory of Key Technology for Rail Traffic Safety, Changsha 410075, China

ARTICLE INFO

*Keywords:*
Superhydrophobic surface coating
Bridge cable icing physics
Cable icing mitigation
Aerodynamic characteristics of iced bridge cable

ABSTRACT

An experimental study is conducted to evaluate the effectiveness of utilizing a superhydrophobic surface (SHS) coating to mitigate ice accretion on bridge cables and to characterize the resultant aerodynamic forces acting on bridge cables under different icing conditions. Two bridge cable models (i.e., a model with untreated hydrophilic surface and a model with SHS coated surface) were used for a comparative study. The dynamic ice accretion process and the resultant aerodynamic forces acting on the bridge models were found to change significantly after applying the SHS coating to treat the cable surface. Under glaze icing condition, the SHS coated cable model was found to have much narrower ice coverage, less amount of accreted ice mass, and smaller aerodynamic drag forces, in comparison to that with untreated cable surface. While the SHS coating was found to be less effective for icing mitigation under rime icing condition, the much rougher rime ice grains accumulated within the droplet direct impinging zone on the SHS coated cable surface caused a greater reduction of the aerodynamic drag forces acting on the cable model at the initial stage of the rime icing process. The acquired ice accretion images were correlated with aerodynamic force measurements for a better understanding of the underlying physics in the context of bridge cable icing mitigation.

## 1. Introduction

It has been found that the cables of cable-stayed bridges are more likely to vibrate under certain weather conditions [1-6]. Bridge cables would encounter icing events frequently in cold environment. Ice accretion over bridge cable surfaces has been found to alter the outer profiles and surface roughness substantially, resulting in great changes in the aerodynamic characteristics of the cables [7]. Ice accretion on bridge cables was also found to cause the uncertainty of cable vibrations and pose safety threats to the bridges as well as the people and vehicles passing the bridges [8]. As a result, some cable-stayed bridges were forced to close due to cable icing. For example, Øresund Bridge over Øresund strait between Sweden and Denmark was reported to close six times due to snow and ice accretion between 2000 and 2010 [9].

In recent years, numerous studies have been carried out to investigate the ice accretion and the resultant aerodynamic characteristics on bridge cables. For example, Giuliani et al. [10] and Demartino et al. [11] conducted wind tunnel testing to quantify the effects of ice accumulation over bridge hangers and stay cables on their aerodynamic characteristics. They reported that the ice layers accumulated on bridge cables altered the cable geometric shapes and increased surface roughness substantially, causing significant effects on their aerodynamic characteristics. Demartino and Ricciardelli [8] applied galloping models to examine the aerodynamic stability of ice-accreted stay cables. The experimental study performed by Koss et al. [12] revealed that test conditions (e.g., different temperatures and the diameters of the cable models) would influence the thermodynamic solidification process and icing characteristics greatly, resulting in different types of ice structures accreted on the cable surfaces. More recently, Górski et al. [13] and Peng et al. [14] measured the airflow fields around iced cable models by using Particle Image Velocimetry (PIV) systems, and found that ice accretion on cable surfaces would induce mode changes of the wake vortex shedding from two sides of the cable models, thereby, affecting the wake flow characteristics significantly. It was also found that commonly used

* Corresponding author.
*E-mail address:* huhui@iastate.edu (H. Hu).

https://doi.org/10.1016/j.expthermflusci.2021.110573
Received 2 June 2021; Received in revised form 27 November 2021; Accepted 29 November 2021
Available online 3 December 2021

surface modifications to bridge cables (e.g., adding helical fillets or making pattern-indented surface structures) would interfere the icing process and the resultant aerodynamic characteristics of the cables [12,14,15].

While extensive studies were conducted for icing mitigation and protection of various engineered structures, such as wind turbines [16,17], aircraft [18,19], and aero-engines [20,21], very little can be found in literature to explore anti-/de-icing methods designed specifically for bridge cable icing mitigation. While Qu & Liu [22] and Laforte et al. [23] summarize the approaches used for the anti-/de-icing operation of power transmission lines, however, those methods may not be directly applied to bridge cables due to the great differences in the functions, surface materials, and configurations of the power transmission lines from those of the bridge cables. It is highly desirable to explore effective and robust anti-/de-icing methods tailored specifically for bridge cable icing mitigation to ensure the safety of cable-stayed bridges in cold climates.

As summarized in Parent and Ilinca [24], all anti-/de-icing strategies are generally categorized as active methods and passive methods, based on whether external energy inputs are needed for the anti-/de-icing operation or not. Active anti-/de-icing approaches (i.e., the approaches requiring external energy inputs) usually include thermal methods (e.g., electric-thermal heating [17], hot air injection [21], and plasma heating [25,26]), chemical spray methods [27], and mechanical techniques [23,28]. While surface heating methods have been demonstrated to be most effective for anti-/de-icing operations, they usually have high power demanding and may also cause damages to the surface materials due to overheating.

A number of passive anti-icing approaches (i.e., the approaches without the no requirements for external energy input) were also developed in recent years to prevent or delay ice accretion on structure surfaces, which include painting surfaces in black to absorb solar energy for icing suppression [24], adding anti-icing fillers in the structure outer layers to delay ice formation [10], and applying hydro-/ice-phobic coatings to prevent water accumulation and/or delay ice formation [16,19,29,30]. Due to much easier implementation and good economy, the passive methods of utilizing hydro-/ice-phobic coatings are attracting increasing attentions for anti-/de-icing of various engineering structures.

Extensive studies have been conducted recently to develop coatings to make Super-Hydrophobic Surface (SHS), on which water droplets bead up with a very large contact angle (i.e., $> 150°$) and drip off rapidly when the surface is slightly inclined [31-36]. In addition to the extraordinary water-repellency, one attractive feature of SHS is the potential to reduce accumulation of snow and ice on solid surfaces [37]. It was found that SHS coated surfaces can delay/suppress ice accumulation at temperatures down to $-30\ °C$ [38,39]. It was also reported that SHS can be icephobic as well with the ice adhesion strength on SHS coated surfaces being only about 10% of that without the SHS coatings [30,40-42]. The experimental study of Waldman and Hu [43] revealed clearly that, corresponding to the superhydrophobic nature and smaller ice adhesion strength over SHS coated surfaces, the aerodynamic shear stress exerted by the incoming airflow would more readily sweep away impinged water mass and accreted ice structures from SHS coated airfoil/wing surfaces under a typical glaze icing condition. As a result, a much less ice coverage was observed over the SHS coated wing surface, in comparison to the case without using the SHS to treat the airfoil/wing surface. More recently, Liu et al. [19] carried out an explorative study to leverage a SHS coating to effectively suppress ice accretion over the surface of a rotating propeller model under different icing conditions. Gao et al. [17] also demonstrated a hybrid anti-/de-icing system by integrating a SHS coating with a minimal surface heating at the airfoil leading edge to effectively prevent ice accretion over the entire surface of an airfoil model at a much lower power cost than the current brutally-forcing surface heating methods. Zhang et al. [44] conducted an experimental campaign to evaluate the mechanical durability of a SHS coating, i.e., the ability to prevent the coating material wearing away from the substrate caused by the continuous impingement of water droplets at high impacting speeds up to 100 m/s.

In the present study, we report an experimental study to examine the effectiveness of utilizing a SHS coating to suppress/delay the icing process on typical bridge cables under different icing conditions. The experimental study was carried out by leveraging the unique Icing Research Tunnel available at Iowa State University (i.e., ISU-IRT). Two bridge cable models with the same geometric dimensions but different surface features (i.e., one model without any surface treatment, and the other coated with a SHS coating) were used for a comparative study. During the experiments, in addition to using a high-speed imaging system to record the dynamic icing process on the surfaces of the cable models with and without SHS coating, three-dimensional (3D) shapes of the ice structures accreted over the test models were measured quantitatively by a 3D scanning system based on a Digital Image Projection (DIP) technique. Meanwhile, a pair of high precision force balances were also used to quantify the time evolutions of the aerodynamic forces acting on the cable models under different test conditions. The recorded ice accretion images and measured 3D shapes of the accreted ice structures were correlated with the aerodynamic force measurements in order to elucidate the underlying physics for a better understanding of how the SHS coating would affect the dynamic ice accretion process and the resultant aerodynamic forces acting on the bridge cables.

## 2. Experimental setup and test model

### 2.1. Icing research tunnel used for the experimental study.

As shown schematically in Fig. 1, the experimental campaign was conducted in the Icing Research Tunnel of Iowa State University (i.e., ISU-IRT). Table 1 summarizes the primary working parameters of ISU-IRT, which include the dimension of the test section, wind speed and temperature, the liquid water content (*LWC*) level, and the size of the airborne supercooled water droplets in ISU-IRT for the icing experiments. By using ISU-IRT, extensive icing and anti-/de-icing studies have been carried out in recent years for various engineering applications [14,15,21,45,46]. For the present study, ISU-IRT was used to generate typical wet glaze and dry rime icing conditions experienced by bridge cables. At the given testing conditions, the temperature distributions inside the test section were found to be quite uniform and stable with the temperature fluctuations being less than 1.0 °C, as measured by using thermocouple probes.

### 2.2. Bridge cable models for the experimental study

Two bridge cable models with identical geometric shapes and dimensions were made for a comparative study. As shown in Fig. 2, the test models used in the present study are full-scale bridge cables with the outer diameter of 82 mm (i.e., $D = 82$ mm) and outer protective material (i.e., high-density polyethylene - HDPE) [8,12,47]. While Model C#1 has the original HDPE surface (i.e., without any surface treatment) and is used as the comparison baseline, Model C#2 is coated with a typical SHS coating in order to examine the effectiveness of using the SHS coating for bridge cable icing mitigation.

A commercially available SHS coating - Hydrobead® was used in the present study to coat the surface of Model C#2. By utilizing a wet film gauge, the SHS coating thickness on the surface of Model C#2 was measured to be about 25 μm. Fig. 3 shows typical images of water droplets on the surface of a HDPE test plate before and after applying the SHS coating. As revealed in Fig. 3(a), the static contact angle of the water droplet on the original HDPE surface was found to be about 75° with a relatively large wetted area, indicating that the untreated HDPE surface of Model C#1 is hydrophilic, similar as that reported by Chalkia et al. [48]. As shown clearly in the Scanning Electron Microscope (SEM) image for the SHS coated surface in Fig. 3(b), after spraying SHS coating

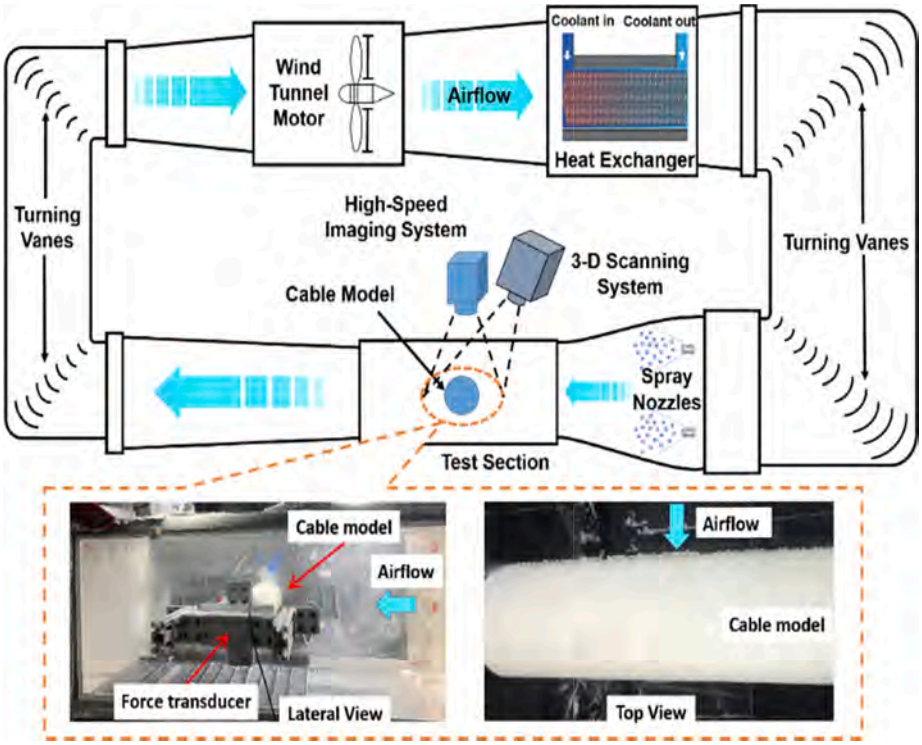


**Fig. 1.** Schematic diagram to show a cable model mounted inside ISU-IRT.

**Table 1**
Primary working parameters of ISU-IRT used in the present study.

| Parameter name | Parameter values or range |
|---|---|
| Width × height × length | 400 mm × 400 mm × 2,000 mm |
| Wind speed | 0 ~ 60 m/s |
| Airflow temperature | −25 °C ~ 25 °C |
| *LWC* level | 0.1 ~ 5.0 g/m$^3$ |
| Water droplets size | 10 ~ 100 μm |

onto the HDPE surface, nano-/micro-scale textures were generated, which would lead to the superhydrophobicity. It was found that the static contact angle of a sessile droplet on the SHS coated surface was approximately 160° with much smaller wetted area. The results showed clearly that the original hydrophilic surface (i.e., untreated HDPE surface) would be changed into superhydrophobic surface by applying the SHS coating. Based on the SEM measurements, while the surface roughness over the uncoated HDPE surface was found to be ~ 2.0 μm (Ra ≈ 2.0 μm), the corresponding value over the SHS coated surface was found to be ~ 1.0 μm (i.e., Ra ≈ 1.0 μm).

### 2.3. Testing parameters and icing conditions

It is well known that, depending on the ambient temperature and the liquid water content (*LWC*) level in the airflow, icing events can usually be categorized into two different kinds of ice accretion process, i.e., rime and glaze icing, with very distinguishable features [49,50]. While Rime icing usually occurs when the airflow is relatively dry (i.e., at relatively small *LWC* level) and the ambient temperature is lower (i.e., below −8.0 °C), glaze icing takes place when the ambient temperature is relatively warm (i.e., −8.0 °C < $T_\infty$ less than 0 °C) and the airflow is relatively wet (i.e., at high *LWC* levels). While accreted rime ice is usually milky-white and opaque with crystalline structures, glaze ice is transparent and glassy, accompanied with evident surface water runback, as reported in Ma et al. [42].

In the present study, the cable models mounted inside ISU-IRT would be exposed to both glaze and rime icing conditions. The primary controlling parameters of the test cases are summarized in Table 2. For the glaze icing experiments, while the *LWC* level in the airflow was set to *LWC* = 2.0 g/m$^3$, the ambient temperature in test section of ISU-IRT was maintained at $T_\infty$ = −5.0 °C. The *LWC* level was reduced to *LWC* = 1.0 g/m$^3$ and ambient temperature decreased to $T_\infty$= −15.0 °C for the rime

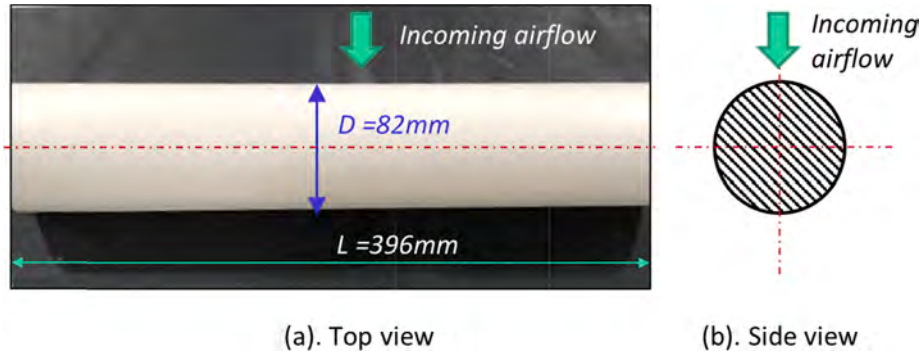


**Fig. 2.** The dimension of the test cable models.

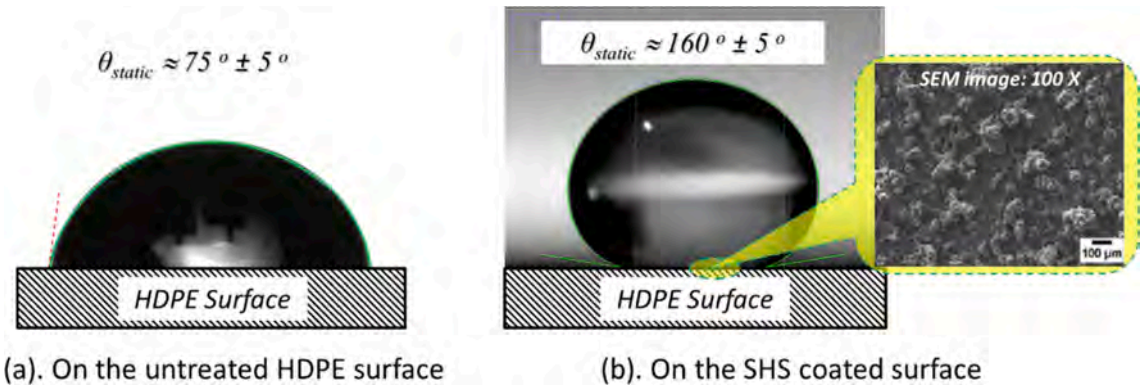


**Fig. 3.** Water droplets siting on original HDPE surface and SHS coated surface.

**Table 2**
Primary controlling parameters of the test cases.

| Case no. | Cable model | $U_\infty$ [m/s] | $T_\infty$ [℃] | $LWC$ [g/m$^3$] | Expected ice type | High speed imaging | 3D scan | Force measurement |
|---|---|---|---|---|---|---|---|---|
| 1 | C#1 | 20 | −5.0 | 2.0 | Glaze | 0 ~ 600 s | at 600 s | 0 ~ 600 s |
| 2 | C#2 | 20 | −5.0 | 2.0 | Glaze | 0 ~ 600 s | at 600 s | 0 ~ 600 s |
| 3 | C#1 | 20 | −15.0 | 1.0 | Rime | 0 ~ 600 s | at 600 s | 0 ~ 600 s |
| 4 | C#2 | 20 | −15.0 | 1.0 | Rime | 0 ~ 600 s | at 600 s | 0 ~ 600 s |

icing experiments. During the experiment, the incoming airflow velocity in the ISU-IRT was maintained at $U_\infty = 20.0$ m/s for all the test cases. The corresponding Reynolds number based on the cable diameter, $Re_D$, and the incoming airflow velocity is about $1.3 \times 10^5$, which is within the range when cable icing events were observed for cable-stayed bridges [12,14,51].

### 2.4. Measurement systems used for the icing experiments

Fig. 4 shows the schematic of experimental setup used in the present study. The cable model was installed in the center of the test section of ISU-IRT with the incoming airflow approaching the test model horizontally. The gaps between the side walls of the ISU-IRT and the two ends of the test model were set to be 2.0 mm. A high-resolution digital imaging system (i.e., PCO Tech, Dimax Camera, 2 K pixels × 2 K pixels in resolution) was mounted above the test section to record of the dynamic icing process over the surface of the cable model. The image spatial resolution was found to be about 0.12 mm/pixel for the present experimental study.

In the present study, a 3D scanning system based on digital image projection (DIP) technique [14,52,53] was also used to achieve "in-situ" measurements of the 3D shapes of the iced cable models. The DIP system is based on the principle of structured light triangulation in a fashion similar to stereo vision technique, but replacing one of the cameras in the stereo pair with a digital projector [54]. A digital image with known pattern characteristics was projected onto the test object of interest (i.e.,

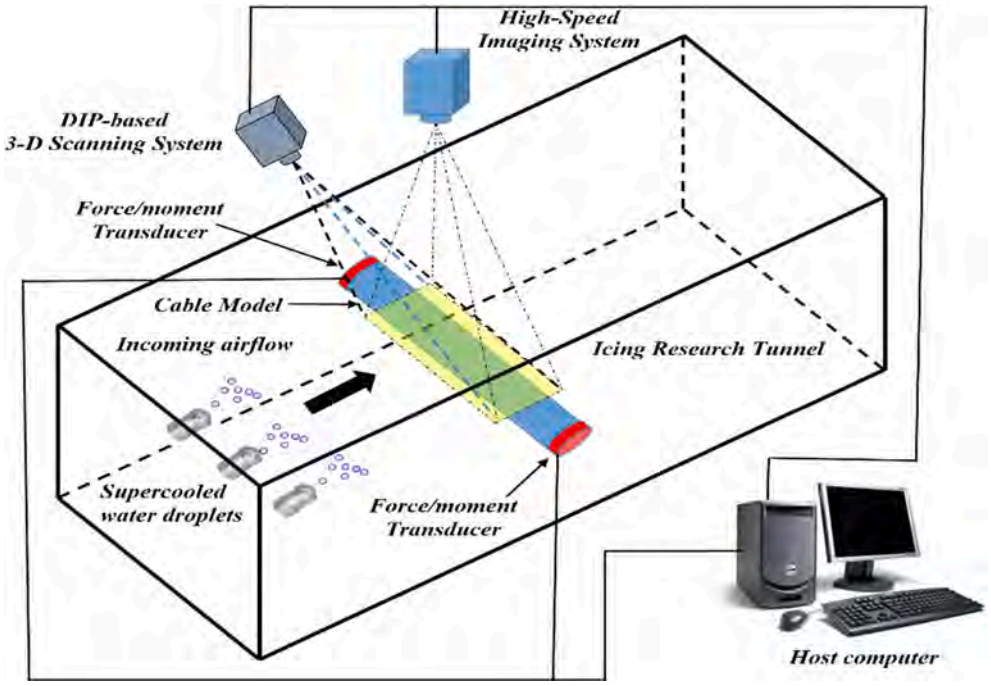


**Fig. 4.** Experimental setup used for the present study.

ice structures accreted over the surface of the bridge cable model for the present study). Due to the complex three-dimensional (3D) geometrical profiles of the test objects (i.e., the surface of the accreted ice structures), the projected digital patterns are deformed when observed from a perspective different from the projection axis. By comparing the distorted digital patterns (i.e., acquired images with ice structures accreted over the surface of the bridge cable model) with a reference digital pattern without the test objects on the reference surface, the 3D profile of the iced test model can be retrieved quantitatively. Further information about the technical basis and implementation of the DIP system is available in Zhang et al. [54] and Gao et al. [52].

After conducting a careful calibration operation to register the correlation relationship between the digital projector and high-resolution camera, the iced cable model was rotated at every 30°around its center for the DIP image acquisitions. The DIP images were processed to retrieve 3D profiles of the ice structures acquired at different phase angles, and then combined automatically to reconstruct the 3D shapes of the ice structures accreted on the test model. For the measurement results given in the present study, the field of view for the 3D scanning system were set to be 200 mm by 200 mm near the midspan of the test models. During the 3D scanning operation, while the airflow in the ISU-IRT was paused, the ambient temperature was kept at the same level as the ice accretion experiment. While it usually takes about 20 s to scan the 3D shapes of the ice structures accreted over the surface of the test model for each test case, the change in the morphology of the accreted ice structures is believed to be very small due to the scanning operation. Based on the results of a calibration procedure similar as that reported in Veerakumar et al. [55], the measurement accuracy of the DIP-based 3D scanning system was found to be about 0.20 mm in measuring 3D shapes of the ice structures accreted over the test models.

During icing experiment, two sets of high-sensitive force/moment transducers (ATI-IA Mini 45) were mounted at 2 ends of the test model to measure the aerodynamic forces acting on the model. The force/moment transducers were connected to a 16-bit data acquisition system (NIUSB-6218) for synchronous data acquisition at the data sample rate of 2,000 Hz. The precision of the force/moment transducers for the force measurements is ± 0.25% of the full range (40 N). The effects of the model blockage, the wake interferences, wind tunnel walls and the additional blockage effects due to the ice accretion on the aerodynamic force measurements were corrected by following the procedures described in Barlow et al. [56].

Before starting the icing experiments, aerodynamic force measurements and 3D scanning of the "clean" cable models (i.e., without any ice accretion over the model surface) were performed, and the measurement results were used as the comparison baseline for the data analysis. The high-speed imaging system was synchronized with the force/moment transducers for the aerodynamic force measurements during the icing experiments of 600 s for each case. The DIP-based 3D scanning of the accreted ice structures was carried out right after finishing the icing experiment.

## 3. Measurement results and discussions

### 3.1. Comparisons of wettability and ice adhesion over untreated and SHS coated surfaces

Before performing ice accretion experiments, an experimental study was conducted to characterize the surface wettability and ice adhesion strength on untreated hydrophilic HDPE surface and SHS coated surface. Surface wettability refers the water repellency of a solid surface, which is usually expressed by static contact angle (CA), $\theta_{static}$; receding CA, $\theta_{rec}$; and advancing CA, $\theta_{adv}$, of water droplets on the surface. Following up the work of Korhonen et al [57], the CA values on the SHS coated surface and untreated HDPE surface were measured by utilizing a needle-in-the-sessile-drop method by placing sessile water droplets (~50 μL deionized water in volume) on the surfaces of the two cable models. The receding CA, $\theta_{rec}$ and advancing CA, $\theta_{adv}$ were measured by contracting and expanding the water droplets at a rate of 10 μL/s over the test surfaces, similar as those reported by Zhang et al. [44]. To minimize the measurement errors, the CA measurements were repeated 10 times. The uncertainty of contact angle measurements was found to be approximately ± 5°.

Table 3 shows the measured CA values on the two compared surfaces. The measured CA values of the present study on the untreated HDPE surface and SHS coated surface were found to agree well with those reported in the previous studies [19,58]. As listed in Table 2, the corresponding contact angle hysteresis (CAH) values, i.e., CAH = $\theta_{adv}$ - $\theta_{rec}$, are also given in the table. It should be noted that CAH value is usually used to indicate the surface slipperiness, i.e., the tendency of water droplets to bounce and/or roll off the surface. The CAH value on the SHS coated surface (i.e., CAH ≈ 5°) was found to be much smaller than that over the HDPE surface (i.e., CAH ≈ 50°). For the bridge cable icing scenario, a cable surface with a smaller CAH value is highly desirable, since it would imply more readily rolling away of water droplets from the cable surface, thereby, less ice accretion on the cable surface [59].

In order to provide a more quantitative comparison about the effects of the surface wettability on cable icing process, especially for glaze icing process, capillary forces (i.e., $F_{capillary}$) that resist water droplets moving over the two compared surfaces were estimated based on the theoretical model used in Liu et al. [19], which is expressed as:

$$F_{capillary} \approx \pi R \gamma_{LG} \left[ sin\left(\frac{\theta_{adv} - \theta_{rec}}{2}\right) sin\left(\frac{\theta_{adv} + \theta_{rec}}{2}\right) \right] \quad (1)$$

where $\gamma_{LG}$ represents the liquid–gas surface tension at the contact line, and $R$ represents the spherical cap radius of the droplet. $\theta_{adv}$ and $\theta_{rec}$ are the advancing and receding CA, respectively. Based on Eq. (1) and measured advancing and receding CA values listed in Table 3, the capillary force ratio of water droplets on the SHS coated surface to those on the original HDPE surface was estimated, which is expressed as:

$$\frac{F_{\text{capillary,SHS}}}{F_{\text{capillary,HDPE}}} \approx \frac{\left[ sin\left(\frac{\theta_{adv}-\theta_{rec}}{2}\right) sin\left(\frac{\theta_{adv}+\theta_{rec}}{2}\right) \right]_{SHS}}{\left[ sin\left(\frac{\theta_{adv}-\theta_{rec}}{2}\right) sin\left(\frac{\theta_{adv}+\theta_{rec}}{2}\right) \right]_{HDPE}} < 0.10 \quad (2)$$

It can be seen clearly that, in comparison to those over the bridge cables with untreated, hydrophilic HDPE surfaces, the capillary forces acting on the water droplets with the same spherical cap radius on the SHS coated surface would much smaller (i.e., less than 10% of that on the untreated HDPE surface). It indicates that, in comparison to those on the bridge cables with untreated HDPE surfaces, much smaller external forces would be needed to overcome the smaller capillary forces to make water droplets rolling off and shedding away from the SHS coated cable surfaces. It also implies that, as driven by the same incoming airflow under the same icing condition, the unfrozen water droplets/rivulets are expected to move much faster over the SHS coated cable surface than those over the untreated HDPE surface, which would enable the runback water to shed off much quicker from the SHS coated bridge cables before frozen into ice on the cable surfaces. All these effects would result in less ice accretion on the bridge cables coated with the SHS coating, which was confirmed by the results of the icing experiment to be discussed later.

**Table 3**
Measured CA values and ice adhesion strength over the compared surfaces.

| Compared Surface | Static CA $\theta_{static}$ [°] | Advancing CA $\theta_{adv}$ [°] | Receding CA $\theta_{rec}$ [°] | CA Hysteresis CAH [°] | Ice adhesion Strength, $\tau_{ice}$ [kPa] |
|---|---|---|---|---|---|
| HDPE | 75 | 80 | 30 | 50 | 600 |
| SHS | 160 | 162 | 157 | 5 | 100 |

By using a similar measurement technique as described in Meuler et al. [60], the ice adhesion strengths, $\tau_{ice}$, on the untreated HDPE surface and SHS coated surface were also measured, and the measurement results are also listed in Table 3 for comparison. For the ice adhesion strength measurements, 3D-printed cylindrical-shaped ice molds (i.e., 8.0 mm in diameter) filled with 0.5 mL deionized water in each mold were used to generate ice samples on test plates with uncoated HDPE surface or SHS coated surface. The test plates were firmly attached to a digitally controlled Peltier cooler (TETech CP061) in a temperature-controlled climate chamber. After the test plates were maintained at the pre-selected frozen-cold temperature (e.g., at −10 °C for all the test cases of the present study) for over 1.0 h, a linear actuator with integrated motion controller (Newport CONEX-LTA-HS) was used to drive a force-torque transducer (JR3-30E12A4) mounted to an aluminum force probe to push the ice molds with a translation velocity of 0.5 mm/s until the ice samples were sheared off completely from the test plates [60]. The ice adhesion strength was then taken as the maximum force-per-area observed as ice samples were sheared off [61]. The ice adhesion measurements were repeated 5 times for each test case. The uncertainty for the ice adhesion measurements was estimated to be ± 20 kPa.

As shown in Table 3, the measured ice adhesion strength on the untreated HDPE surface was found to be ~ 600 kPa, which agree with the measurement results reported in Moncholi [62]. In comparison, the ice adhesion strength on the SHS coated surface was found to be about 100 kPa, which is only about 15% of the value on the untreated HDPE surface. It confirms that the SHS coating used in the present study is also

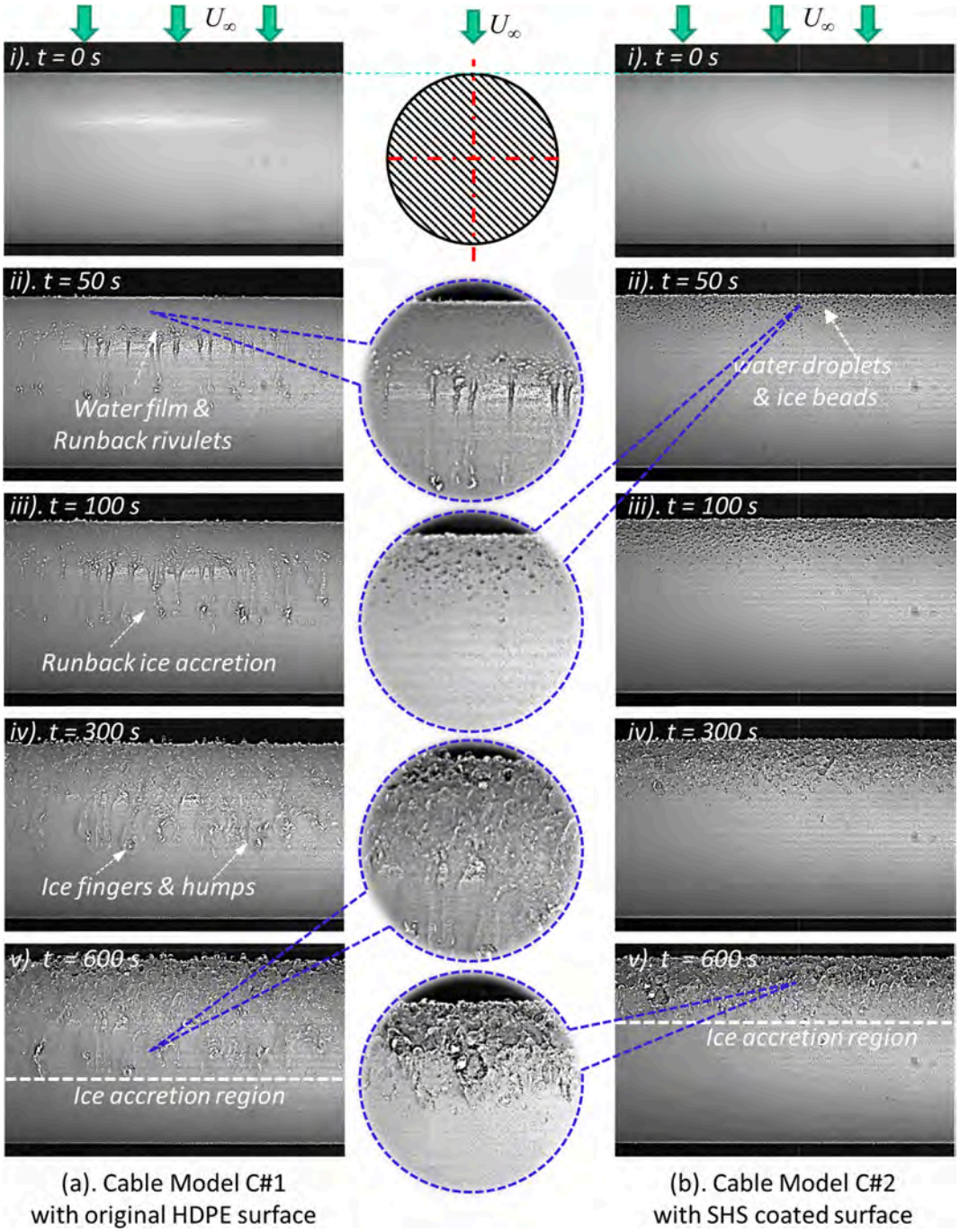


**Fig. 5.** Time evolution of the ice accretion process on the two compared cable models under the glaze icing conditions of $U_\infty = 20$ m/s, $T_\infty = -5$ ℃, and $LWC = 2.0$ g/m$^3$.

icephobic. It is worth noting that the ice adhesion strength over a solid surface would indicate the easiness to remove the accreted ice from the surface. The smaller ice adhesion strength on the SHS coated surface would imply that, even for the situation that bridge cable icing had already occurred, the ice structures accreted on SHS coated cable surfaces would be much easier to be removed or blown away by the aerodynamic shear forces exerted by the incoming airflow, in comparison to those accreted on the bridge cables with untreated HDPE surface. It should be noted that, the ice samples used for the adhesion strength measurements over the compared surfaces were generated under relatively static icing conditions with the substrate temperature being at −10 °C. The ice adhesion measurement results would be applicable to make a fair comparison between different surfaces, especially for the runback icing process beyond the direct impinging zone of the water droplets on the cable surface.

### 3.2. High-speed imaging results to reveal the effects of SHS coating on the ice accretion process

An experimental campaign was carried out to reveal the effects of SHS coating on the dynamic ice accretion process over the surfaces of the bridge cable models under typical rime and glaze icing conditions. Before starting the icing experiments, the ISU-IRT was operated at the prescribed frozen-cold temperature levels (e.g., $T_\infty = -5$℃ for the glaze icing, and $T_\infty = -15$℃ for the rime icing) for at least 30 min before switching on the water spray system to ensure that ISU-IRT reached a thermal steady state. After the aerodynamic forces acting on "clean" cable models (i.e., without any ice structures accreted on the cable models) were measured, the water spray system was then turned on to start the ice accretion experiments.

Fig. 5 shows typical snapshot images to reveal the dynamic ice accretion process over the surfaces of the two compared test models under the glaze icing condition of $U_\infty = 20$ m/s, $T_\infty = -5$ ℃, and $LWC = 2.0$ g/m$^3$. While the acquired images given in the left column (i.e., Fig. 5(a)) are for Model C#1 with untreated HDPE surface, the right column lists the results of Model C#2 with the SHS coated cable surface (i.e., Fig. 5 (b)). Similar as described in Waldman and Hu [63], after turning on the water spray system of ISU-IRT at the time of $t = 0$, micro-sized water droplets exhausted from the water spray atomizers would be cooled down rapidly and become airborne, supercooled water droplets. The super -cooled water droplets carried by the frozen-cold airflow would impinge onto the front surfaces of the cable models to start the ice accretion process. Similar as that described in Liu et al. [19], since the impingement of supercooled water droplets was found to concentrate mainly within narrow regions near the leading edges of the cable models (i.e., the direct impacting zone of the supercooled water droplets), ice accretion was observed on the front surfaces of the cable models at first, as revealed clearly from the snapshot images acquired at the beginning of the icing experiments (i.e., at $t = 50$ s). Due to the inadequate heat transfer to remove/dissipate the released latent heat of fusion associated with the solidification (i.e., icing process) under such a wet glaze icing condition (i.e., with a relatively warm ambient temperature of $T_\infty = -5.0$ ℃ and high $LWC$ level of $LWC = 2.0$ g/m$^3$), only a portion of the supercooled water droplets were observed to be frozen into ice, upon impacting onto the cable surfaces, while the rest of the impacted water mass was found to stay in liquid phase over the cable surface.

As shown clearly in Fig. 5(a), for Model C#1 with untreated HDPE surface, due to the relatively large wetted area of the impacted water droplets associated with small CA values on the hydrophilic HDPE surface, the unfrozen water droplets were found to coalesce rapidly to form a thin water film on the front surface of cable model, as shown clearly in the snapshot image acquired at $t = 50$ s. Driven by the aerodynamic forces exerted by the incoming airflow over the cable surface, the unfrozen water was found to run back along the cable surface, resulting in the formation of multiple rivulets to transport the impacted water mass from the cable front surface to further downstream locations, as shown clearly in the snapshot image acquired at $t = 100$ s. Since the incoming airflow was at the frozen temperature of $T_\infty = -5.0$ ℃ during the icing experiment, the runback water would be cooled down continuously as flowing to further downstream regions. As a result, the runback water was found to be frozen into ice eventually to form runback ice structures at the downstream locations (i.e., outside the direct impinging zone of the water droplets). As shown clearly in the snapshot images acquired after $t = 300$ s, the shapes of the runback ice structures accreted on the untreated HDPE surface were found to become very complex with the formation of rivulet-shaped ice fingers and humps. As the ice accretion time increases, while the thickness of the ice layer accreted on the cable front surface was found to increase greatly, much more runback ice structures were observed to accrete over the backside of the cable surface. The shapes of the ice structures accreted on the cable surface were also found to become much more complicated. Irregular-shaped ice fingers and humps were found to grow outward rapidly and extrude further into the incoming airflow, which would catch more airborne supercooled water droplets to further accelerate the growth of the ice accretion. It should be noted that, the formation of irregular-shaped glaze ice structures on the cable surface would affect the aerodynamic performance of the cable model significantly, which was revealed quantitatively from the aerodynamic force measurements to be discussed later. In summary, ice structures accreted on Model C#1 were found to exhibit typical features of glaze icing, i.e., forming transparent, glassy ice structures with obvious traces of water runback, as described in Hansman and Kirby [50].

The effects of the SHS coating on the glaze ice accretion process over the cable surface were revealed very clearly from the acquired ice accretion images given in Fig. 5(b). Due to the superhydrophobic nature of the SHS coated surface, the impacted water droplets on the front surface of Model C#2 were found to bead up rapidly, instead of coalescing to form a water film as that on the hydrophilic HDPE surface revealed in Fig. 5(a). The water droplets siting on the front surface of the Model C#2 were found to be frozen into isolated ice beads subsequently, since they were exposed into the frozen-cold airflow. In comparison to the scenario over the untreated HDPE surface of Model C#1, while much less ice was found to accrete on the cable front surface, no runback water or ice accretion was observed on the backside of the SHS coated cable Model C#2. The much less glaze ice accretion on the SHS coated Model C#2 is believed to be caused by following reasons: with the same amount of supercooled water droplets impinging onto the cable surface, the water droplets would more readily bounce off and roll away from the SHS coated surface, due to the much smaller CA hysteresis of the water droplets on the SHS coated surface. As a result, much smaller amount of impinged water would be able to accumulate on the SHS coated cable surface, leading to much less ice accretion on the SHS coated cable surface, in comparison to that on the untreated, hydrophilic HDPE surface. Furthermore, under the glaze icing condition, since only a portion of the impacted water mass would be frozen into ice upon impacting onto the cable surface, the remaining unfrozen water would run back as driven by the incoming airflow over the cable surface. Due to the much slippery nature of the SHS coated surface (i.e., the magnitudes of the capillary forces to resist moving of the water droplets/rivulets on the SHS coated surface are less than 10% of those on the hydrophilic HDPE surface), the unfrozen surface water would run back much faster and shed off from the SHS coated cable surface before being frozen into ice. Therefore, no runback ice accretion was observed on the backside of the SHS coated cable surface. Even for the case with ice structures happened to accrete on the cable surface, since the ice adhesion strength over the SHS coated surface is much smaller than that on the untreated HDPE surface (i.e., being only about 15% of that on the untreated HDPE surface), the aerodynamic shear forces exerted by the incoming airflow would more readily sweep the accreted ice structures away from the SHS coated cable surface. All these would contribute to the much less ice accretion on the SHS coated cable model under the glaze icing condition, as revealed clearly in Fig. 5(b).

It should also be noted that, even though the ice accretion on the SHS coated cable model was found to become much less than that on the uncoated HDPE surface, ice structures were still found to accrete on the front surface of Model C#2, especially near the cable leading edge (i.e., in the vicinity of the stagnation line). This highlights one of the major challenges facing by the strategies using hydro-/ice-phobic coatings for cable icing mitigation. While hydro-/ice-phobic coatings, including the SHS used in the present study, can effectively reduce the adhesion forces between the impacted water droplets or/and accreted ice and cable surface, they rely on aerodynamic forces acting tangentially to the cable surfaces to remove the accumulated water/ice structures. Such approaches would break down near the front stagnation line because the aerodynamic shear forces near the stagnation lines would be very small or vanish completely. As a result, impinged water droplets would stay on the SHS coated cable surface and were frozen into ice subsequently.

Furthermore, as shown clearly in Fig. 3, SHS coated surfaces would possess nano-/micro-scaled textured or roughness structures on the surfaces. When a macroscopic water droplet comes in contact with a textured SHS coated surface, it usually adopts so-called ***Cassie-Baxter state*** [64] with air trapped inside the surface texture beneath the droplet. Since the macroscopic water droplet is supported on thousands of pockets of air, it beads up and displays very high contact angles (>150° for SHS). However, for the cable icing scenario, supercooled water droplets carried by the incoming airflow would impact onto the cable front surface at a relatively high impacting speed of $U_\infty = 20$ m/s, the impacted water droplets would easily penetrate into the surface textures, completely wetting the pores or asperities of the surface textures to make the impacted water droplets in so-called ***Wenzel state***

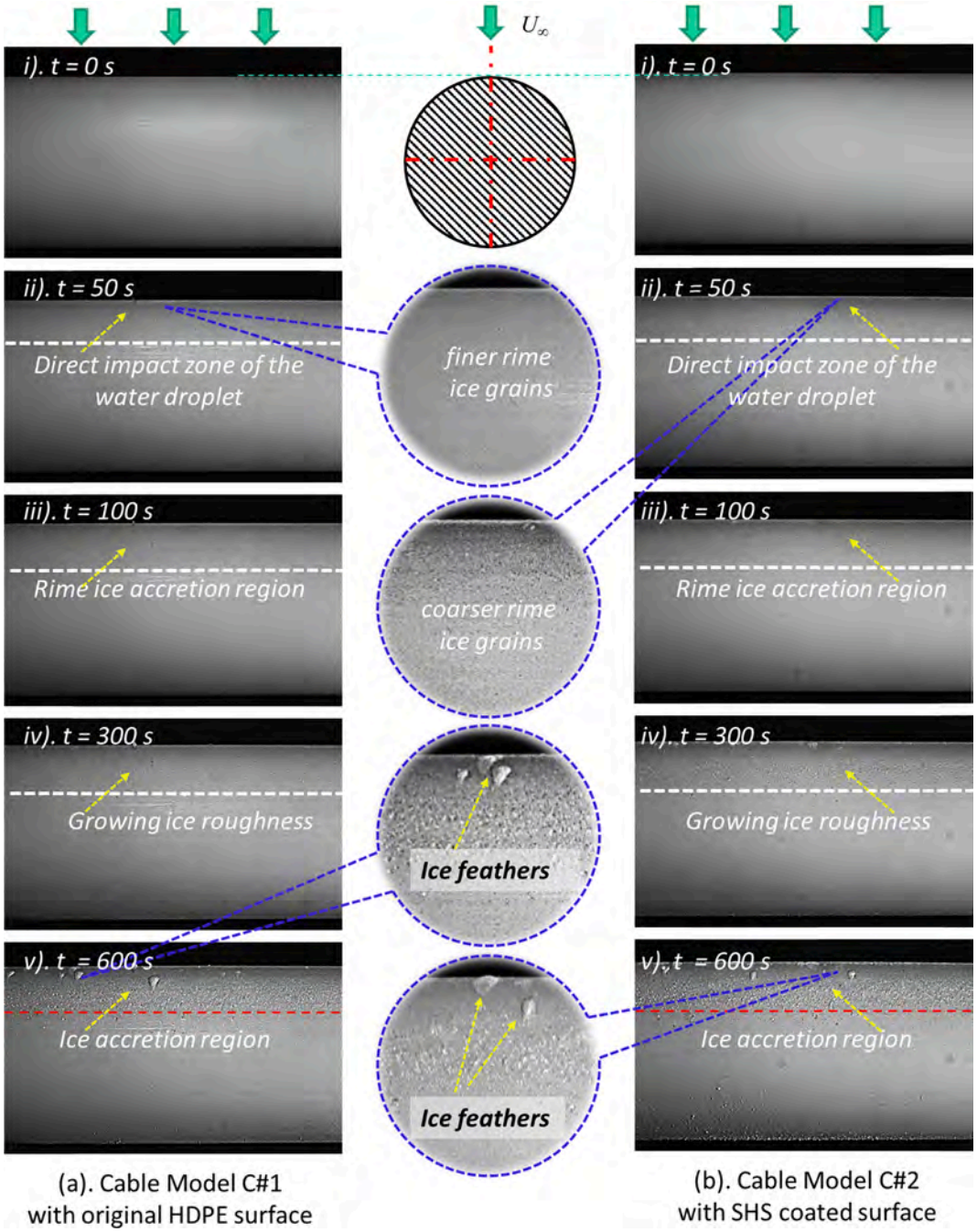


**Fig. 6.** Time evolution of the ice accretion process over the surfaces of the two compared cable models under the rime icing conditions of $U_\infty = 20$ m/s, $T_\infty = -15$ ℃, and $LWC = 1.0$ g/m$^3$.

[65]. Once the impacted water was frozen within the nano-/micro-scale surface textures (i.e., in the Wenzel state), it would be extremely difficult to remove the ice structures, even more than those on non-textured surfaces, because of the interlocking effects between ice and the surface textures [66]. This would also contribute the ice accretion on the front surface of Model C#2. Once ice started to accrete on the front cable surface, next groups of the supercooled water droplets would impact directly onto the surface of the ice layer, instead of the SHS coated surface. Therefore, as the time increases, more and more ice structures were found to accrete on the front surface of the SHS coated cable model, as shown clearly in Fig. 5(b).

Fig. 6 shows the acquired snapshot images of the ice accretion processes over the two compared cable models under the typical rime icing condition of $T_\infty = -15$ ℃, and $LWC = 1.0$ g/m$^3$. Similar as that described in Liu & Hu [67], since the airflow in the ISU-IRT was set at a much colder temperature with the *LWC* level being only half of the glaze icing case described above, the heat transfer (i.e., including both conductive and convective heat transfer) under such a colder and drier testing condition would become much more efficient to rapidly remove/dissipate the released latent heat of fusion associated with the solidification (i.e., icing process) of the fewer impacted water mass on the cable surfaces. While the supercooled water droplets were found to be frozen into ice instantly upon impacting onto the cable surfaces, no traces of unfrozen water runback were observed on the cable surfaces. Therefore, no ice accretion was found on the backside of the cable models (i.e., beyond the direct impinging zone of the supercooled water droplets), as revealed clearly from the acquired snapshot images given in Fig. 6.

Due to the almost instantly freezing of the impacted supercooled water droplets under the rime icing condition, air bubbles/pockets would be trapped inside the voids between the rime ice grains accreted on the cable models. Therefore, the ice structures accretion over the front surfaces of the cable models were found to be opaque and have milk-white appearance, which exhibits typical rime ice characteristics as described in Hansman and Kirby [50]. As ice accretion time increases, while the ice layers accreted along the leading edges of the cable models were found to become thicker and thicker, the surfaces of the iced cable were also found to be much rougher. Some noticeable ice "feathers" were found to grow on the cable front surfaces at the late stage of rime icing process, as shown clearly in the images acquired at $t = 300$ s and $t = 600$ s.

As revealed clearly from the side-by-side comparison of the acquired ice accretion images given in Fig. 6, the rime ice accretion characteristics on the SHS coated cable surface of Model C#2 were found to be very similar to those of Model C#1 with untreated HDPE surface in general. Based on a more careful comparison of the ice accretion images acquired at the earlier stage of the rime icing experiments (i.e., $t \leq 100$ s), the ice structures accreted on the SHS coated surface were found to have coarser ice grains than those on the hydrophilic HDPE surface. This can be explained by the fact that the impacted supercooled water droplets on the SHS coated surface would be more likely to bead up due to the superhydrophobic nature of the SHS coated surface. The differences in the accreted ice grain size/roughness were found to be much less distinguishable at the later stage of the rime icing experiments (i.e., $t \geq 300$ s) with continuous impingement of supercooled water droplets onto the surface of the accreted ice layer, instead of the SHS coated cable surface.

In summary, the SHS coating was found to have much less effects on the rime icing process in comparison to the glaze icing process. This can be explained by the facts that, upon the impingement of the supercooled water droplets onto the cable front surface, the impacted water droplets on the SHS coated surface would be more readily changed from the partially-wetted *Cassie-Baxter state* to the fully-wetted *Wenzel state*, eliminating the icephobicity of the SHS surface greatly [68]. Furthermore, the aerodynamic forces exerted by the boundary layer airflow over the cable front surface, especially near the stagnation line of the cable model, are usually very small or vanished completely. As a result, the impacted water droplets sitting on the front surface of Model C#2 would be frozen into ice rapidly under such a colder rime icing condition. Once water freezes within the surface textures of SHS coated surface (i.e., in the Wenzel state), it would be very difficult to remove the accreted ice because of the interlocking between ice and the surface textures as described in Lv et al. [69]. Therefore, the SHS coating was found to be less effective in mitigating rime ice accretion over the cable surface, as shown clearly in Fig. 6.

### 3.3. 3D scanning results to quantify the ice structures accreted on the cable models

In addition to using the high-speed imaging system to qualitatively visualize the dynamic ice accretion processes on the surfaces of the cable models with and without SHS coating, a DIP-based 3D scanning system was also used in the present study to quantify the 3D shapes of the ice structures accreted on the cable models at the end of the icing experiments (i.e., at $t = 600$ s). Fig. 7 and Fig. 8 give the measurement results to characterize the 3D shapes of the ice structures accreted on the cable surfaces under the wet glaze and dry rime icing conditions. Based on the 3D scanning measurement results, the cross-sectional profiles of the iced cable models at any cross-section locations can be extracted. Typical profiles of the ice layers accreted over the cable surfaces, which were extracted in arbitrarily selected cross-sections near the midspans of the cable models, were shown in Fig. 7 and Fig. 8. The average profiles of the ice layers accreted over the cable surfaces, which were obtained by averaging the measured ice profiles in 20 cross-sections along the cable span for each test case, were also given in Fig. 7 and Fig. 8 for comparison. The effects of the SHS coating on the ice accretion characteristics over the cable surfaces were revealed clearly and quantitatively based on the comparison of the measurement results.

As revealed clearly from the 3D scanning results given in Fig. 7, the ice structures accreted over the surfaces of the cable models under the glaze icing condition were found to be rather rough in general. The complex features of the glaze ice structures revealed from the 3D scanning results were found to correlate well with the formation of large-scale runback ice fingers and humps over the cable surfaces as visualized qualitatively from the snapshot images acquired during the glaze icing process given in Fig. 5.

As described above, after impinging onto the hydrophilic HDPE surface of Model C#1, while only a portion of the impinged supercooled water droplets would be frozen into ice under the glaze icing condition, the rest of the impinged water was found to coalesce rapidly to form a water film over the cable front surface. Driven by the aerodynamic shear force exerted by the incoming airflow, the unfrozen water film was found to run back, flowing into the downstream region on the backside of the cable model. As a result, the impinged water mass was transported from the cable front surface to much further downstream locations and frozen into ice subsequently, causing the much greater coverage of the accreted ice layer on Model C#1. As shown quantitatively from the 3D scanning results given in Fig. 7(a) and Fig. 7(c), while the "averaged" profile of the accreted ice layer over the cable model was found to be much smoother than the typical ice profile extracted from "single" cross-section near the cable midspan, the upper and lower limits identified based on the "averaged" ice profile were found to be consistent with those revealed from the ice profile extracted from the "single" cross-section near the cable midspan. More specifically, while the upper limit of the ice layer accreted on Model C#1 was found to extend to the downstream location of $\theta_{upper} \approx 115^\circ$, the lower limit of the ice layer reached to the azimuthal angle of $\theta_{lower} \approx -110^\circ$.

Since the incoming airflow were set to be perpendicular to the direction of the gravity force for the present icing experiments, the effects of the gravity force on the runback of the unfrozen water over the upper surface of the cable model would be different from those over the lower cable surface. Due to the gravity effects, the runback water film over the lower surface of Model C#1 was found to more readily break into

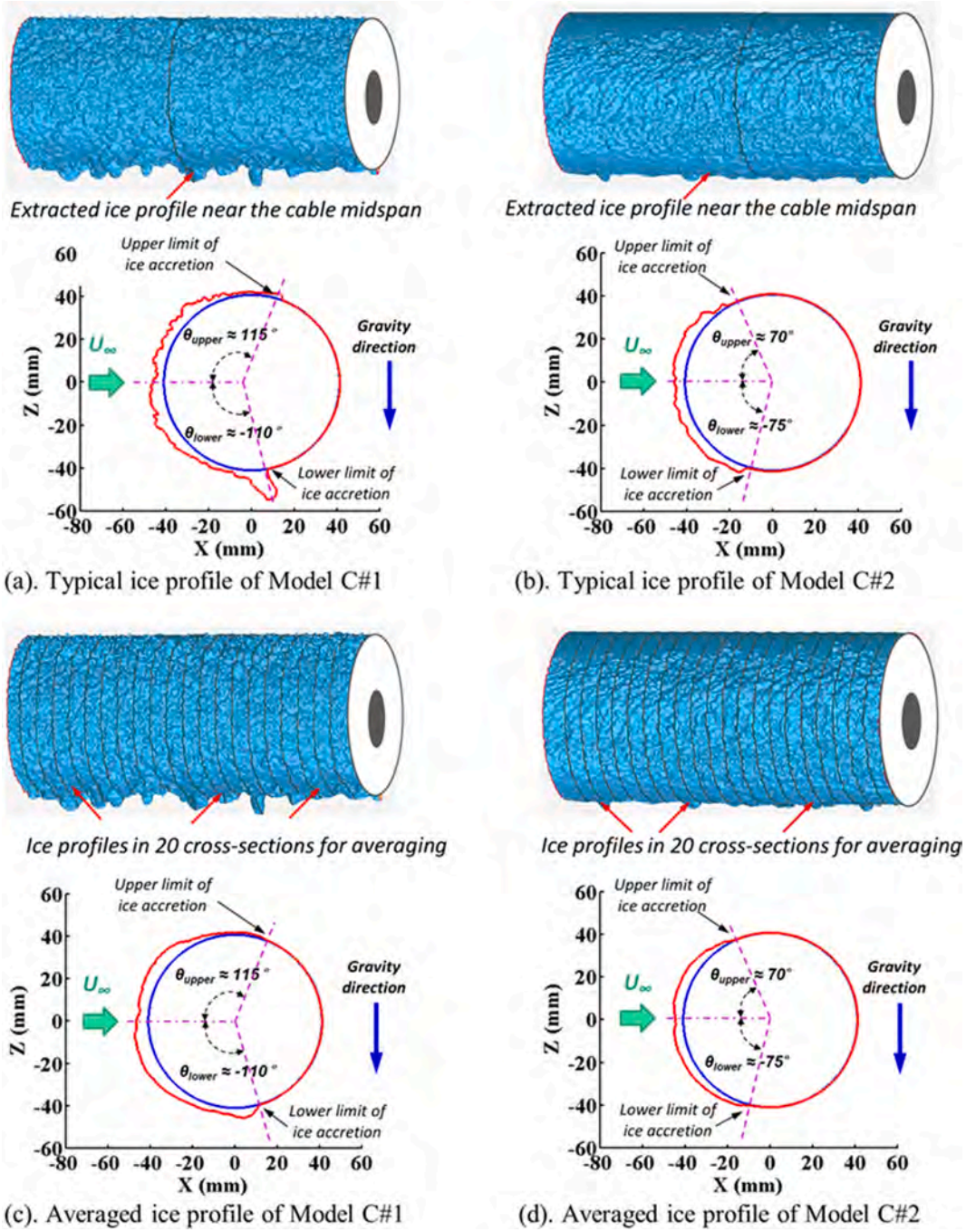


**Fig. 7.** 3D scanning results of the glaze ice structures accreted on the cable models after 600 s of the icing experiments.

rivulets and freeze into complicated ice structures, in comparison to that over the cable upper surface. As shown clearly in Fig. 7(a), the irregular-shaped runback ice structures accreted over the cable lower surface were found to intrude further into the incoming airflow, which would cause large-scale separation of the airflow from the cable surface. This would result in greater aerodynamic drag forces acting on the cable model, which was confirmed quantitatively from the force measurement results to be discussed later.

The 3D scanning results given in Fig. 7(b) and Fig. 7(d) reveals clearly that, even though the two compared cable models were exposed to the same glaze icing condition, the outer profiles of the glaze ice layer accreted on the SHS coated surface of Model C#2 was found to become significantly different from that on Model C#1. Since the much smaller capillary forces acting on the water droplets/rivulets over the SHS coated surface would enable more readily rolling off of the runback water, and the weaker ice adhesion would also ensure easier shedding of the accreted ice from the SHS coated surface, the coverage of the ice layer accreted on the Model C#2 was found to become much less than that over Model C#1. It confirms that the SHS coating is very effective to mitigate glaze ice accretion over the cable surface. It can also be observed that, due to the different gravity effects on the water transport process over the upper and lower surfaces of the cable models, more glaze ice structures were found to accrete over the lower cable surface. While the upper limit of the ice layer accreted over the SHS coated surface of Model C#2 were found to end at the azimuthal angles of $\theta_{upper} \approx 70°$, the coverage of the ice layer on the lower cable surface was found to extend to $\theta_{lower} \approx -75°$ due to the gravity effects. In summary, after applying the SHS coating to the cable surface, the coverage of the ice

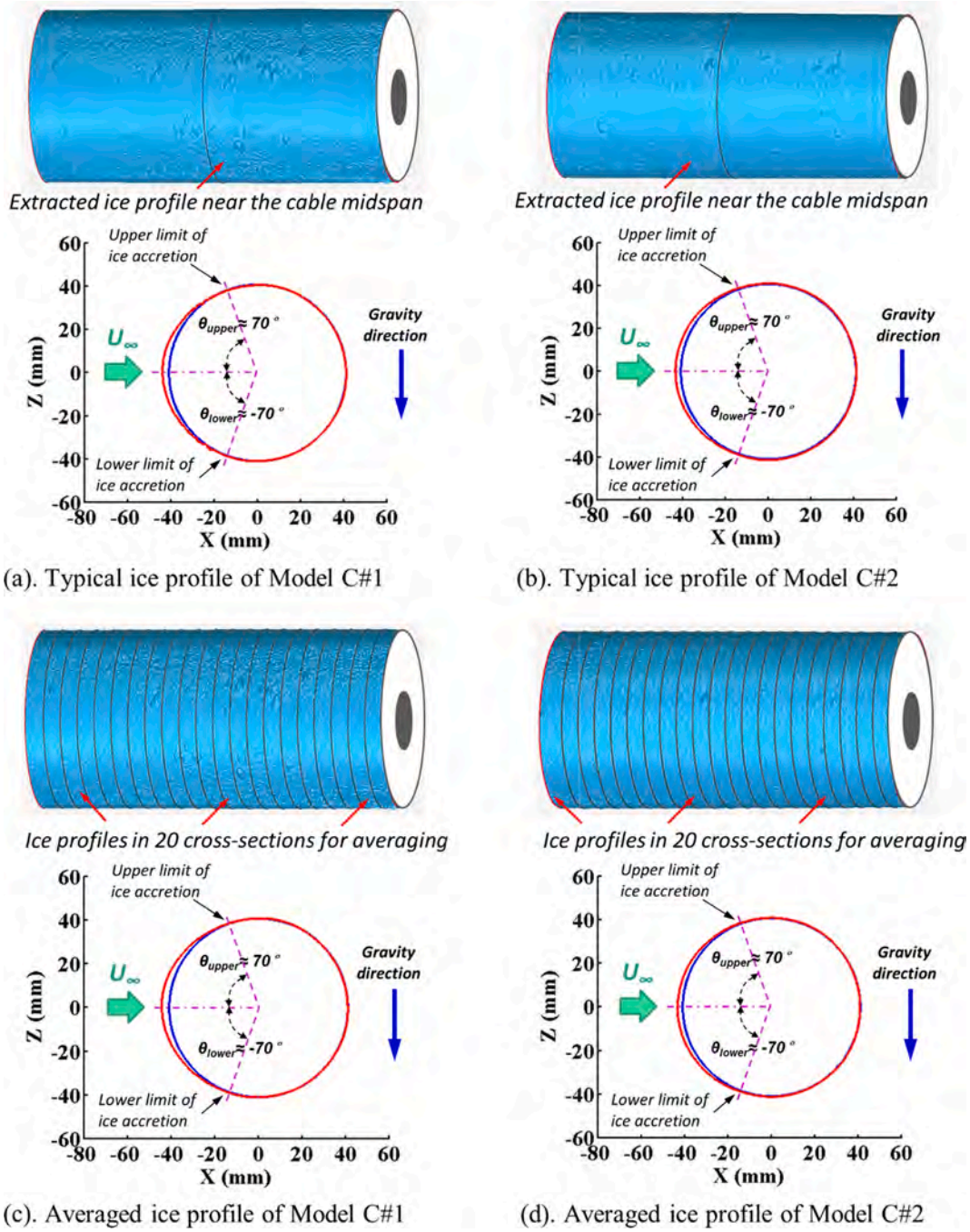


**Fig. 8.** 3D scanning results of the rime ice structures accreted on the cable models after 600 s of rime icing experiments.

layer on the cable model was found to be reduced by about 40% under the glaze icing condition.

As aforementioned, under the typical rime icing condition of $U_\infty$ = 20 m/s, $T_\infty = -15$ ℃, and $LWC = 1.0$ g/m$^3$, upon impacting onto the cable surfaces, the supercooled water droplets were found to be frozen into ice instantly with no runback water existing over the cable surfaces, thereby, no ice formation on the backsides of the cable models. As revealed quantitatively from the 3D ice shape scanning results given in Fig. 8, the rime ice structures accreted on the cable surfaces were found to be restricted on the front cable surface only, i.e., mainly within the direct impinging zone of the supercooled water droplets. It can also be seen that, while the ice layers accreted near the cable leading edges (i.e., at the front stagnation points) were found to have the greatest thickness, the ice layer thickness was found to decrease monotonically as the azimuthal angle increases. The upper and lower limits of the rime ice layers accreted on the cable surfaces were found to end at the azimuthal angles of $\theta_{upper} \approx 70°$ and $\theta_{lower} \approx -70°$, respectively.

The distribution characteristics of the rime ice layers accreted over the cable surfaces were found to be closely related to the impingement characteristics of the airborne supercooled water droplets onto the cable models. As described in Anderson & Tsao [70], rime ice accretion process would be affected mainly by the collection efficiency characteristics of the supercooled water droplets carried by the incoming airflow. Corresponding to the highest water collection efficiency at the cable leading edges (i.e., the front stagnation points), the rime ice layer accreted on the cable models was found to reach the maximum thickness at the cable leading edge, and then decrease gradually at further downstream locations. As a result, the shapes of the iced cable models

were found to be elongated along the incoming airflow direction. As shown clearly in Fig. 8, with the continuous accretion of rime ice on the cable front surfaces, the outer profiles of the iced cable models were found to become more "streamlined" in shape, in comparison to the original circular shape. The more streamlined shapes of the iced cable models would lead to smaller aerodynamic forces acting on the cable models, which was confirmed quantitatively from the aerodynamic force measurement results to be discussed in the later section.

Based on the side-by-side comparison of the 3D scanning results for the two compared cable models given in Fig. 8, it can be seen clearly that the outer profile of the rime ice layer accreted over the SHS coated surface of Model C#2 was found to be almost the same as that of Model C#1 with hydrophilic HDPE surface. The findings agree well with the features revealed from the acquired ice accretion images given in Fig. 6. It indicates again that the SHS coating would be much less effective to mitigate rime ice accretion over cable surface, due to instant solidification of the supercooled water droplets upon impacting onto the cable surface under the rime icing condition. It should also be noted that, as shown clearly in Fig. 8, the rime ice layers accreted over the cable surfaces were found to be almost symmetric in relation to the incoming airflow direction, indicating that the gravity force would have almost no effects on the rime icing process.

Based on the quantitative 3D scanning results given in Fig. 7 and Fig. 8, total volumes of the ice layers accreted over the surfaces of the cable models within the measurement window (i.e., within the 200 mm midspans of the test models) can also be determined, i.e., by subtracting the volumes of the "clean" cable models (i.e., without any ice accretion) from the measured total volumes of the iced cable models. As reported in Liu et al. [71], while the density of typical glaze ice is usually about 900 kg/m$^3$, the density of typical rime ice is slightly less, i.e., about 880 kg/m$^3$, due to the entrainment of more air bubbles between rime ice grains. Therefore, the total ice mass accreted on the two compared cable models can also be determined quantitatively.

Table 4 summarizes the measured ice mass accreted on the two compared cable models after 600 s of the ice accretion experiments under both the rime and glaze icing conditions. It can be seen clearly that, the total mass of the glaze ice accreted on Model C#2 (i.e., with the SHS coated cable surface) was found to be only about 70% of that accreted on Model C#1 (i.e., with untreated hydrophilic HDPE surface), indicating ~ 30% reduction in the accreted ice mass due to the SHS coating. However, the total mass of the rime ice accreted on the SHS coated cable model C#2 was found to be only slightly less (i.e., ~3% reduction in the accreted ice mass) than that on the cable model with untreated HDPE surface. It indicates again that the passive anti-icing method of using SHS coatings for cable icing mitigation would be more effective under the wet glaze icing condition with warmer temperatures, in comparison to that under the dry rime icing condition with much colder ambient temperatures.

It should be noted that the $LWC$ level in the incoming airflow for the glaze icing experiments (i.e., $LWC = 2.0$ g/m$^3$) was set to be 2.0 times of that of the rime icing experiments (i.e., $LWC = 1.0$ g/m$^3$). However, after the same ice accretion duration of 600 s, while the total mass of the ice accumulated on Model C#1 with untreated HDPE surface under the glaze icing condition was found to be about 3.2 times of that of the rime icing case. The corresponding value was found to become about 2.3 times for the cases of Model C#2 with SHS coated surface. The significant differences in the ice mass accumulated on the cable surface under the rime and glaze icing conditions were believed to be closely related to the different characteristics of the dynamic ice accretion process on the cable surface under different icing conditions. As aforementioned, while glaze ice accretion occurred over much wider areas and formed much more complicated ice structures (i.e., ice fingers and humps) due to the existence of unfrozen runback water over the cable surfaces, rime icing took place only within the droplet direct impacting zone on the front cable surfaces. Under the glaze icing condition, the irregular-shaped ice structures accreted over the cable surfaces were found to protrude further into the incoming airflow, which would catch extra airborne water droplets to further accelerate the glaze ice accretion over cable surfaces.

**Table 4**
Comparison of the accreted ice mass on the cable models.

| Cable model | After 600 s of the glaze icing experiment (Kg/m) | After 600 s of the rime icing experiment (Kg/m) |
|---|---|---|
| C#1 | 0.493 | 0.157 |
| C#2 | 0.352 | 0.153 |

### 3.4. Aerodynamic characteristics of the cable models during dynamic ice accretion process

As mentioned above, the unsteady aerodynamic forces acting on the cable models were also measured before and during the icing experiments. The aerodynamic forces acting on the "clean" cable models (i.e., without ice accretion) were used as the comparison baseline to evaluate the effects ice accretion on the aerodynamic characteristics of the cable models. Since the measured lift forces acting on the cable models (i.e., vertical component of the aerodynamic forces) were found to be always very small in comparison to the drag forces (i.e., the horizontal component of the aerodynamic forces), the present study would focus primarily on the variations of the drag forces acting on the cable models during the ice accretion process.

The drag coefficient of a cable model (i.e., $C_d$) is usually defined by:

$$C_d = \frac{F_d}{\frac{1}{2}\rho U_\infty^2 DL} \tag{3}$$

where $F_d$ is the measured drag force acting on the test model; $\rho$ is the density of airflow; $U_\infty$ is freestream velocity of the incoming airflow; $D$ is the diameter of the cable model; and $L$ represents the spanwise length of the cable model. The drag coefficients of the "clean" cable models before starting the icing experiment (i.e., $C_{d\_no\_ice}$) were found to be about 0.95, which is in good agreement with those reported in Kleissl and Georgakis [47] at the same Reynolds number levels. It should be noted that the measured drag coefficients of the cable models with and without SHS coating were found to be almost the same (i.e., $< \pm 3\%$) before starting the ice accretion experiments. In the present study, the $F_{d\_no\_ice}$ is used as the baseline to evaluate the effects of the dynamic ice accretion process on the aerodynamic drag forces acting on the bridge cable models.

It should be noted that, due to the ice accretion over the cable models, the projected area of the iced cable models along the incoming airflow direction would change dynamically during the ice accretion experiments (e.g., up to 10% increase after 600 s of the glaze ice accretion). Instead of using drag coefficient, normalized drag, which is defined as the measured instantaneous drag acting on the iced cable model normalized by the averaged value of the drag acting on the same cable model before starting the icing experiment (i.e., $F_d/F_{d\_no\_ice}$), was used to characterize the effects of the ice accretion on the aerodynamic drag forces acting on the cable model.

Fig. 9 shows the time evaluations of the measured aerodynamic drag data, i.e., $F_d/F_{d\_no\_ice}$, of the two compared cable models under the glaze icing condition. The Gaussian-filtered mean values (i.e., moving averaged values) based on the instantaneous measurement results were also given in the plot. It can be seen clearly that the time variations of the aerodynamic drag forces acting on the cable models were found to have two evident stages during the glaze icing process, i.e., 1) a rapid drag reduction stage at the beginning of the icing experiment; and 2) a gradual drag increase stage at the later of the glaze icing experiment. Similar features were also observed in the recent study of Veerakumar et al. [14] to study the dynamic icing process over power transmission lines at a much lower Reynolds number level of $Re_D \approx 50{,}000$.

As shown clearly in Fig. 9, while the aerodynamic drag acting on

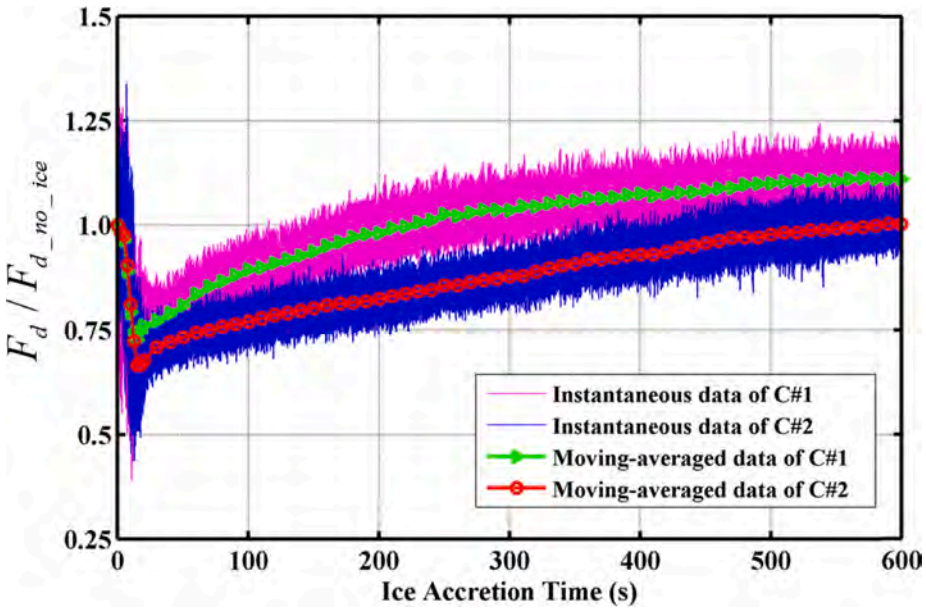


**Fig. 9.** Measured aerodynamic drag data during the glaze ice accretion process.

Model C#1 (i.e., with untreated HDPE surface) was found to decreased by approximately 20% within the first 20 s of glaze icing experiment, the corresponding values for Model C#2 was found to become even less, i.e., decreased by about 30%. As suggested by Veerakumar et al. [14], at the initial stage of the glaze icing process (i.e., within the first 20 s of the glaze icing process for the present study), while the ice layers accreted on the cable models were still very thin, the existence of runback water films on the cable front surfaces would affect the development of the boundary layer airflow over the cable surfaces. In comparison to the "dry" cable surface case, the runback water films over the cable surfaces would act as "lubricant layers" to make the airflow moving more smoothly over the "wet" surfaces of the cable models. It would make the "wet" cable surfaces becoming more "slippery" to the incoming airflow than the "dry" cable surfaces. This would delay the separation of the airflow over the cable surfaces, resulting in smaller aerodynamic drag forces acting on the cable models at the initial stage of the glaze ice accretion process.

It should also be noted that, as described clearly in the textbook of Frank White [72], the aerodynamic drag forces acting on cylindrical cable models would be very sensitive to the surface roughness, particularly in the range of $Re_D \approx 1.3\text{x}10^5$ where the measurements of the presents study were conducted. After the ice accretion experiments start, the surfaces of the cable models would become much rougher due to the ice accretion. The fast growth of the surface roughness over the ice accreting cable surfaces would also result in rapid decreases of the aerodynamic drags acting on the cable models, which would also contribute to the quick reduction of the measured aerodynamic drag data at the initial stage of the glaze ice accretion process.

At the later stage of the glaze icing experiment, the aerodynamics drag forces acting on the cable models were found to grow gradually as the ice accretion time increases. The continuous increase of the drag at the second stage is believed to be caused by the thicker and thicker glaze ice layers accreted on the cable surfaces, which would enlarge the projected area of the iced cable models along the incoming airflow direction. It can also be seen that the growth rate of the drag for Model C#2 with SHS coated surface was found to slower than that of Model C#1 (i.e., with hydrophilic HDPE surface) at the second stage of the glaze icing process. In comparison to those acting on Model C#2, the greater aerodynamic drag forces acting on Model C#1 are believed to be closely related to the formation of more complicated, irregular-shaped runback ice structures (i.e., ice fingers and bumps) on the hydrophilic cable surface of Model C#1. As described above, the irregular-shaped runback ice structures were found to protrude further into the incoming airflow to cause large-scale separation of airflow over the cable surface, resulting in the larger aerodynamic drag acting on cable model. After 600 s of the glaze icing experiment, while the mean drag of Model C#1 was found to increase to about 118% of its initial value, the corresponding value for Model C#2 was found to become almost the same as its initial value.

Fig. 10 shows the measured aerodynamic drags of the cable models as a function of the ice accretion time under the rime icing condition. It can be seen clearly that, the variation characteristics of the drags due to the rime ice accretion were found to be significantly different from those under the glaze icing condition. For Model C#1 with untreated HDPE surface, the aerodynamic drag forces acting on the test model was found to decrease monotonously as the ice accretion time increases. After 600 s of the rime icing experiments, the mean aerodynamic drag of the iced cable model was found to become only about 75% of its initial value (i.e., the drag of the "clean" cable model). The decreasing feature of aerodynamic drag forces acting on Mode C#1 is believed to be closely related to the continuous growth of the rime ice layer accreted over the front surface of the cable model to make the outer profile shape of the iced cable model changing gradually from the original circular shape to more streamlined shape, as revealed clearly from the 3D ice shape measurement results given in Fig. 8.

In comparison to those acting on Model C#1 with untreated hydrophilic HDPE surface, the aerodynamic drag force acting on Model C#2 with SHS coated surface was found to decrease much faster at the earlier stage of the rime icing process. After reaching to the minimum mean value of being only about 72% of the initial value (i.e., drag reduction by 28%) at the time of $t \approx 100$ s, the aerodynamic drag forces acting on Model C#2 were found to increase very slowly as the ice accretion time increases. After 600 s of the rime icing experiment, the mean drag of Model C#2 was found to become about 78% of that of the "clean" cable model without any ice accretion, which is almost the same as that of Model C#1. The much faster decrease of the aerodynamic drag forces acting on Model C#2 in the earlier stage of the rime ice accretion process is believed to be closely related to the formation of the much coarser rime ice grains over the front surface of Model C#2 due to the superhydrophobic nature of the SHS coated surface, as revealed from the snapshot images acquired at the beginning of the rime icing process (i.e., $t \leq 100$ s) given in Fig. 6. The coarser rime ice grains formed over the

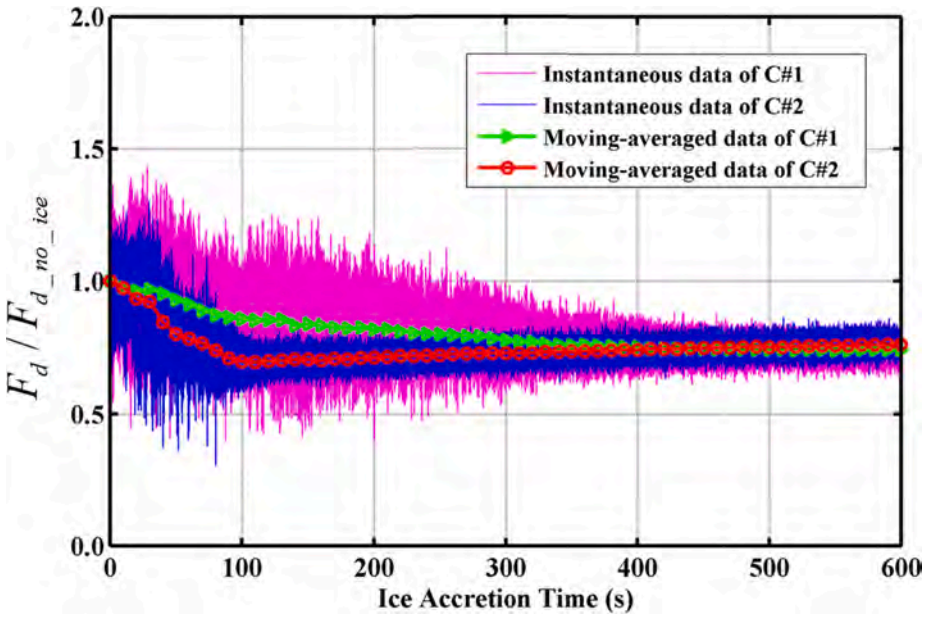


**Fig. 10.** Measured aerodynamic drag data during the rime ice accretion process.

front surface of Model C#2 would act as "turbulators" to promote a faster transition of the laminar boundary layer airflow over the cable surface (i.e., working similarly as the dimples over the surfaces of golf balls), thereby, resulting in the rapid reduction of the aerodynamic drag forces acting on Mode C#2 at the earlier stage of rime ice accretion process. A similar fast transition of the laminar boundary layer airflow induced by ice roughness accreted near the leading edge was also reported by Shin [73]. The finding derived from measured aerodynamic drag data of the present study, i.e., the rapid growth of the surface roughness over the ice accreting cable surfaces would cause a rapid decrease of the aerodynamic drags acting on the cylindrical cable models in the range of $Re_D \approx 1.3 \times 10^5$, was also found to agree well with the results given in the textbook of Frank White [72].

As the ice accretion time increases, much more supercooled water droplets would impinge onto the surface of the accreted ice layer, instead of the SHS surface. Therefore, the differences in the grain sizes of the rime structures accreted on the two compared cable models were found to become much less distinguishable at the later stage of the rime icing process. As a result, the aerodynamic drag forces acting on Model C#2 with the SHS coated surface were found to become almost the same as those acting on Model C#1 with untreated HDPE surface.

## 4. Conclusions

A comprehensive experimental investigation was conducted to evaluate the effects of a SHS coating on dynamic icing process and resultant aerodynamic characteristics of bridge cables exposed to typical glaze and rime icing conditions. The experimental study was performed in an icing research tunnel available at Iowa State University (i.e., ISU-IRT). Two bridge cable models with different surface wettability (i.e., a test model with untreated, hydrophilic HDPE surface, and the other model with SHS coated cable surface) were exposed under the same icing conditions for a comparative study. In addition to using a high-resolution imaging system to record the transient behaviors of the ice accretion process over the cable surfaces, a digital image projection (DIP) based, three-dimensional (3D) scanning system was also used to quantify the 3D shapes of the ice structures accreted over the cable surfaces. The time evolutions of the resultant aerodynamic forces acting on the cable models during the ice accretion process were also measured by using a pair of high-sensitive force/moment sensors mounted at two ends of the cable models.

Under the typical glaze icing condition of $U_\infty = 20$ m/s, $T_\infty = -5.0$ ℃, and $LWC = 2.0$ g/m$^3$, while only a portion of the supercooled water droplets were found to be frozen into ice instantly upon impacting onto the cable surfaces, the rest of the impacted water mass was found to be stay in liquid phase. For the cable model with untreated hydrophilic surface, the unfrozen water was found to coalesce rapidly to form a water film on the cable front surface, and then run back gradually over the cable surface as driven by the frozen-cold incoming airflow. The wind-driven runback of the unfrozen water over the hydrophilic cable surface was found to evolve into multiple rivulets to transport the impinged water mass from the cable front surface to much further downstream locations. The runback water was found to be frozen into ice eventually on the backside of the cable model, resulting in a much greater coverage of the ice layer accreted on the cable surface. Due to the gravity effects, the wind-driven runback water flow over the lower cable surface was found to more readily break into rivulets and freeze subsequently into irregular-shaped ice structures, in comparison to that over the upper cable surface. The irregular-shaped runback ice structures (i.e., ice fingers and humps) were found to grow outward rapidly and extrude further into the incoming airflow, which would catch more airborne supercooled water droplets to further accelerate the growth of the glaze ice structures. The fast growth of the irregular-shaped glaze ice structures accreted on the hydrophilic cable surface induced large-scale airflow separation over the iced cable surface, resulting in greater aerodynamic drag forces acting on the iced cable model.

The glaze ice accretion on the cable model with SHS coated surface was found to be suppressed greatly in comparison to that over the untreated hydrophilic cable surface. More specifically, after 600 s of the glaze icing experiment, while the coverage of the ice layer accreted over the SHS coated cable surface was found to be reduced by 40%, the total accreted ice mass was found to be reduced by about 30%, in comparison to those on the cable model with untreated hydrophilic surface. The resultant aerodynamic drag forces acting on the cable model were also found to decrease by about 18% after applying the SHS coating to cover the cable surface. The much less glaze ice accretion on the SHS coated cable surface is believed to be caused by following reasons: 1). With the same amount of supercooled water droplets impinging onto the cable surface, the impacted water droplets would more readily bounce off and/or roll away from the SHS coated surface, causing much less water accumulating on the SHS coated surface, thereby, less ice accretion on the SHS coated cable model. 2). Due to the much slippery nature of the

SHS coated surface, the wind-driven runback water droplets/rivulets would move much faster over the SHS coated cable surface than those over the untreated hydrophilic surface. Therefore, the unfrozen water would be much more likely to roll off and shed away from the SHS coated cable surface before being frozen into ice. 3). Even for the case with ice structures happed to accrete on the cable surface, the aerodynamic shear forces exerted by the incoming airflow would more readily blow away the accreted ice from the SHS coated cable surface due to the much weaker ice adhesion strength on the SHS coated surface than that on the untreated hydrophilic surface.

Under the typical rime icing condition of $U_\infty = 20$ m/s, $T_\infty = -15.0$ ℃, and $LWC = 1.0$ g/m$^3$, since the supercooled water droplets would be frozen into ice instantly upon impinging onto the cable surfaces, rime ice accretion was found to take place only on the front surfaces of the cable models. No traces of the water runback or ice accretion were observed beyond the direct impinging zones of the water droplets. Corresponding to the highest water collection efficiency at the cable leading edges (i.e., the front stagnation points), the thickness of the accreted rime ice layer was found to reach the maximum value at the cable leading edges, and then decrease gradually at further downstream locations. With the continuous growth of the rime ice layer accreted over the front surface of the cable models, the iced cable models were found to be elongated along the incoming airflow direction, making the outer profiles of the iced cable models to become more "streamlined" in shape, in comparison to the original circular shape. The more streamlined shape due to rime ice accretion resulted in smaller aerodynamic forces acting on the iced cable models.

The SHS coating was found to become much less effective in mitigating rime ice accretion on the cable surface, in comparison to the scenario of glaze icing. The ice structures accreted on the SHS coated cable surface at the earlier stage of the rime icing experiment were found to have much coaster ice grains than those accreted on the hydrophilic cable surface due to its superhydrophobic nature. The much rougher rime ice structures accreted on the cable front surface acted as "turbulators" to promote a fast transition of the laminar boundary layer airflow over the cable front surface, resulting in a rapid reduction of the aerodynamic drag forces acting the SHS coated cable model at the earlier stage of the rime ice accretion process. As the ice accretion time increases, with more and more supercooled water droplets impinging onto the surface of the accreted ice layer, instead of the SHS coated cable surface, the differences in the grain sizes of the rime ice structures accreted on the two compared cable models were found to become much less distinguishable. Therefore, the resultant aerodynamic drag forces acting on the two compared cable models became almost the same at the later stage of the rime icing experiments.

### *CRediT authorship contribution statement*

**Yihua Peng:** Writing – original draft. **Ramsankar Veerakumar:** . **Zichen Zhang:** . **Haiyang Hu:** . **Yang Liu:** Methodology. **Xuhui He:** Funding acquisition, Supervision. **Hui Hu:** Methodology, Formal analysis, Writing – review & editing, Funding acquisition, Supervision.

### Declaration of Competing Interest

The authors declare that they have no known competing financial interests or personal relationships that could have appeared to influence the work reported in this paper.

### Acknowledgements

The first author, YH Peng would like to thank China Scholarship Council to support his visit to Iowa State University. This research work is partially support by National Science Foundation (NSF) of USA under award numbers of IOSE-1826978 and CBET-1916380. The support from National Natural Science Foundation of China (No. U1934209, 51708559, 51925808) and National Key R&D Program of China (subproject 2017YFB1201204) to YH Peng and XH He is also acknowledged.

### References

[1] X.H. He, S. Ai, H. Jing, Energy transmission at subcritical Reynolds numbers for the wake-induced vibration of cylinders in a tandem arrangement, Ocean Eng. 211 (2020), 107572, https://doi.org/10.1016/j.oceaneng.2020.107572.
[2] M. Jafari, F. Hou, A. Abdelkefi, Wind-induced vibration of structural cables, Nonlinear Dyn. 100 (1) (2020) 351–421, https://doi.org/10.1007/s11071-020-05541-6.
[3] D. Zuo, N.P. Jones, Interpretation of field observations of wind- and rain-wind-induced stay cable vibrations, J. Wind Eng. Ind. Aerodyn. 98 (2) (2010) 73–87, https://doi.org/10.1016/j.jweia.2009.09.004.
[4] H. Jing, Y. Xia, H. Li, Y. Xu, Y. Li, Excitation mechanism of rain–wind induced cable vibration in a wind tunnel, J. Fluids Struct. 68 (2017) 32–47, https://doi.org/10.1016/j.jfluidstructs.2016.10.006.
[5] W.L. Chen, X.W. Min, D.L. Gao, A.X. Guo, H. Li, Experimental investigation of aerodynamic forces and flow structures of bionic cylinders based on harbor seal vibrissa, Exp. Therm. Fluid Sci. 99 (2018) 169–180, https://doi.org/10.1016/j.expthermflusci.2018.07.033.
[6] D. Gao, G. Chen, W. Chen, Y. Huang, H. Li, Effects of steady wake-jets on subcritical cylinder flow, Exp. Therm. Fluid Sci. 102 (2019) 575–588, https://doi.org/10.1016/j.expthermflusci.2018.12.026.
[7] A. Benidir, O. Flamand, L. Gaillet, G. Dimitriadis, Impact of roughness and circularity-defect on bridge cables stability, J. Wind Eng. Ind. Aerodyn. 137 (2015) 1–13, https://doi.org/10.1016/j.jweia.2014.11.010.
[8] C. Demartino, H.H. Koss, C.T. Georgakis, F. Ricciardelli, Effects of ice accretion on the aerodynamics of bridge cables, J. Wind Eng. Ind. Aerodyn. 138 (2015) 98–119, https://doi.org/10.1016/j.jweia.2014.12.010.
[9] N. Gimsing, C.T. Georgakis, Cable Supported Bridges: Concept and Design, 3rd editio, Wiley, 2012 https://www.wiley.com/en-us/Cable+Supported+Bridges%3A+Concept+and+Design%2C+3rd+Edition-p-9780470666289.
[10] F. Giuliani, F. Merusi, G. Polacco, S. Filippi, M. Paci, Effectiveness of sodium chloride-based anti-icing filler in asphalt mixtures, Constr. Build. Mater. 30 (2012) 174–179, https://doi.org/10.1016/j.conbuildmat.2011.12.036.
[11] C. Demartino, F. Ricciardelli, Aerodynamic stability of ice-accreted bridge cables, J. Fluids Struct. 52 (2015) 81–100, https://doi.org/10.1016/j.jfluidstructs.2014.10.003.
[12] H.H. Koss, H. Gjelstrup, C.T. Georgakis, Experimental study of ice accretion on circular cylinders at moderate low temperatures, J. Wind Eng. Ind. Aerodyn. 104–106 (2012) 540–546, https://doi.org/10.1016/J.JWEIA.2012.03.024.
[13] P. Górski, S. Pospíšil, M. Tatara, A. Trush, PIV analysis of near-wake flow patterns of an ice-accreted bridge cable in low and moderately turbulent wind, J. Wind Eng. Ind. Aerodyn. 191 (2019) 297–311, https://doi.org/10.1016/j.jweia.2019.06.011.
[14] Y. Peng, R. Veerakumar, Y. Liu, X. He, H. Hu, An experimental study on dynamic ice accretion and its effects on the aerodynamic characteristics of stay cables with and without helical fillets, J. Wind Eng. Ind. Aerodyn. 205 (2020), 104326, https://doi.org/10.1016/j.jweia.2020.104326.
[15] Y. Liu, W. Chen, Y. Peng, H. Hu, An experimental study on the dynamic ice accretion processes on bridge cables with different surface modifications, J. Wind Eng. Ind. Aerodyn. 190 (2019) 218–229, https://doi.org/10.1016/j.jweia.2019.05.007.
[16] L. Ma, Z. Zhang, L. Gao, Y. Liu, H. Hu, An exploratory study on using Slippery-Liquid-Infused-Porous-Surface (SLIPS) for wind turbine icing mitigation, Renew. Energy. 162 (2020) 2344–2360, https://doi.org/10.1016/j.renene.2020.10.013.
[17] L. Gao, Y. Liu, L. Ma, H. Hu, A hybrid strategy combining minimized leading-edge electric-heating and superhydro-/ice-phobic surface coating for wind turbine icing mitigation, Renew. Energy. 140 (2019) 943–956, https://doi.org/10.1016/J.RENENE.2019.03.112.
[18] W. Zhou, Y. Liu, H. Hu, H. Hu, X. Meng, Utilization of thermal effect induced by plasma generation for aircraft icing mitigation, AIAA J. 56 (3) (2018) 1097–1104, https://doi.org/10.2514/1.J056358.
[19] Y. Liu, L. Li, H. Li, H. Hu, An experimental study of surface wettability effects on dynamic ice accretion process over an UAS propeller model, Aerosp. Sci. Technol. 73 (2018) 164–172, https://doi.org/10.1016/j.ast.2017.12.003.
[20] L. Li, Y. Liu, H. Hu, An experimental study on dynamic ice accretion process over the surfaces of rotating aero-engine spinners, Exp. Therm. Fluid Sci. 109 (2019), 109879, https://doi.org/10.1016/J.EXPTHERMFLUSCI.2019.109879.
[21] L. Li, Y. Liu, L. Tian, H. Hu, H. Hu, X. Liu, I. Hogate, A. Kohli, An experimental study on a hot-air-based anti-/de-icing system for aero-engine inlet guide vanes, Appl. Therm. Eng. 167 (2020), https://doi.org/10.1016/j.applthermaleng.2019.114778.
[22] C.-Z. Qu, Y.-J. Liu, De-icing Method for Coupled Transmission Tower-Line System, Energy Procedia 17 (2012) 1383–1389, https://doi.org/10.1016/j.egypro.2012.02.256.
[23] J.L. Laforte, M.A. Allaire, J. Laflamme, State-of-the-art on power line de-icing, Atmos. Res. 46 (1-2) (1998) 143–158, https://doi.org/10.1016/S0169-8095(97)00057-4.
[24] O. Parent, A. Ilinca, Anti-icing and de-icing techniques for wind turbines: Critical review, Cold Reg. Sci. Technol. 65 (1) (2011) 88–96, https://doi.org/10.1016/j.coldregions.2010.01.005.
[25] W. Zhou, Y. Liu, H. Hu, H. Hu, X. Meng, Utilization of thermal effect induced by plasma generation for aircraft icing mitigation, AIAA J. 56 (2018), https://doi.org/10.2514/1.J056358.

[26] Y. Liu, C. Kolbakir, A.Y. Starikovskiy, R. Miles, H. Hu, An experimental study on the thermal characteristics of NS-DBD plasma actuation and application for aircraft icing mitigation, Plasma Sources Sci. Technol. 28 (2019), 014001, https://doi.org/10.1088/1361-6595/aaedf8.
[27] L. Gray, Review of Aircraft Deicing and Anti-Icing Fluid Storm Water Runoff Control Technologies, in: 2013: p. MANE 6960H01 – Air and Water Pollution Prevention. http://www.ewp.rpi.edu/hartford/~grayl3/AWPPCE/Water/Project/Aircraft De-icing Effluent Control Methods-Gray.pdf (accessed February 14, 2016).
[28] D. Li, Z. Chen, Experimental study on instantaneously shedding frozen water droplets from cold vertical surface by ultrasonic vibration, Exp. Therm. Fluid Sci. 53 (2014) 17–25, https://doi.org/10.1016/j.expthermflusci.2013.10.005.
[29] C. Antonini, M. Innocenti, T. Horn, M. Marengo, A. Amirfazli, Understanding the effect of superhydrophobic coatings on energy reduction in anti-icing systems, Cold Reg. Sci. Technol. 67 (1-2) (2011) 58–67, https://doi.org/10.1016/j.coldregions.2011.02.006.
[30] Z.J. Wang, D.J. Kwon, K. Lawrence DeVries, J.M. Park, Frost formation and anti-icing performance of a hydrophobic coating on aluminum, Exp. Therm. Fluid Sci. 60 (2015) 132–137, https://doi.org/10.1016/j.expthermflusci.2014.09.003.
[31] A. Carre, K.L. Mittal, Superhydrophobic surfaces, VSP, Leiden; Boston, 2009.
[32] Y. Cheng, D. Rodak, C. Wong, C. Hayden, Effects of micro-and nano-structures on the self-cleaning behaviour of lotus leaves, Nanotechnology. 17 (2006) 1359–1362. http://iopscience.iop.org/article/10.1088/0957-4484/17/5/032/meta (accessed February 14, 2016).
[33] Y. Liu, X. Chen, J.H. Xin, Hydrophobic duck feathers and their simulation on textile substrates for water repellent treatment, Bioinspir. Biomim. 3 (4) (2008) 046007, https://doi.org/10.1088/1748-3182/3/4/046007.
[34] K. Koch, B. Bhushan, Y. Jung, W. Barthlott, Fabrication of artificial Lotus leaves and significance of hierarchical structure for superhydrophobicity and low adhesion, accessed February 14, 2016, Soft Matter 5 (2009) 1386–1393, http://pubs.rsc.org/en/content/articlehtml/2009/sm/b818940d.
[35] T.-S. Wong, T. Sun, L. Feng, J. Aizenberg, Interfacial materials with special wettability, MRS Bull. 38 (5) (2013) 366–371, https://doi.org/10.1557/mrs.2013.99.
[36] F. Wang, C. Liang, M. Yang, X. Zhang, Effects of surface characteristics on liquid behaviors on fin surfaces during frosting and defrosting processes, Exp. Therm. Fluid Sci. 61 (2014) 113–120, https://doi.org/10.1016/j.expthermflusci.2014.10.022.
[37] P. Zhang, F.Y. Lv, A review of the recent advances in superhydrophobic surfaces and the emerging energy-related applications, Energy. 82 (2015) 1068–1087, https://doi.org/10.1016/j.energy.2015.01.061.
[38] L. Cao, A.K. Jones, V.K. Sikka, J. Wu, D.i. Gao, Anti-icing superhydrophobic coatings, Langmuir 25 (21) (2009) 12444–12448, https://doi.org/10.1021/la902882b.
[39] L. Mishchenko, B. Hatton, V. Bahadur, J.A. Taylor, T. Krupenkin, J. Aizenberg, Design of ice-free nanostructured surfaces based on repulsion of impacting water droplets, ACS Nano 4 (12) (2010) 7699–7707.
[40] Z. Hu, X. Wu, F. Chu, X. Zhang, Z. Yuan, Off-centered droplet impact on single-ridge superhydrophobic surfaces, Exp. Therm. Fluid Sci. 120 (2021), 110245, https://doi.org/10.1016/j.expthermflusci.2020.110245.
[41] Z. Zhang, L. A, H. Hu, X. Bai, H. Hu, An experimental study on the detrimental effects of deicing fluids on the performance of icephobic coatings for aircraft icing mitigation, Aerosp. Sci. Technol. 119 (2021) 107090. 10.1016/J.AST.2021.107090.
[42] L. Ma, Z. Zhang, L. Gao, Y. Liu, H. Hu, Bio-inspired icephobic coatings for aircraft icing mitigation: a critical review, Rev. Adhes. Adhes. 8 (2) (2020) 168–199, https://doi.org/10.7569/RAA.2020.097307.
[43] R.M. Waldman, H. Li, H. Hu, An Experimental Investigation on the Effects of Surface Wettability on Water Runback and Ice Accretion over an Airfoil Surface, in: 8th AIAA Atmos. Sp. Environ. Conf., American Institute of Aeronautics and Astronautics, Virginia, 2016. 10.2514/6.2016-3139.
[44] Z. Zhang, L. Ma, Y. Liu, J. Ren, H. Hu, An experimental study of rain erosion effects on a hydro-/ice-phobic coating pertinent to Unmanned-Arial-System (UAS) inflight icing mitigation, Cold Reg. Sci. Technol. 181 (2021), 103196, https://doi.org/10.1016/j.coldregions.2020.103196.
[45] L. Gao, Y. Liu, H. Hu, An experimental investigation on the dynamic glaze ice accretion process over a wind turbine airfoil surface, Int. J. Heat Mass Transf. 149 (2020), 119120, https://doi.org/10.1016/J.IJHEATMASSTRANSFER.2019.119120.
[46] Y. Liu, L. Ma, W. Wang, A.K. Kota, H. Hu, An experimental study on soft PDMS materials for aircraft icing mitigation, Appl. Surf. Sci. 447 (2018) 599–609, https://doi.org/10.1016/j.apsusc.2018.04.032.
[47] K. Kleissl, C.T. Georgakis, Comparison of the aerodynamics of bridge cables with helical fillets and a pattern-indented surface, J. Wind Eng. Ind. Aerodyn. 104–106 (2012) 166–175, https://doi.org/10.1016/j.jweia.2012.02.031.
[48] V. Chalkia, N. Tachos, P.K. Pandis, A. Giannakas, M.K. Koukou, M. G. Vrachopoulos, L. Coelho, A. Ladavos, V. Stathopoulos, Influence of organic phase change materials on the physical and mechanical properties of HDPE and PP polymers, RSC Adv. 8 (48) (2018) 27438–27447.
[49] S. Fukusako, A. Horibe, M. Tago, Ice accretion characteristics along a circular cylinder immersed in a cold air stream with seawater spray, Exp. Therm. Fluid Sci. 2 (1) (1989) 81–90, https://doi.org/10.1016/0894-1777(89)90052-6.
[50] R.J. Hansman, M.S. Kirby, Comparison of wet and dry growth in artificial and flight icing conditions, J. Thermophys. Heat Transf. 1 (3) (1987) 215–221, https://doi.org/10.2514/3.30.
[51] P. Gorski, S. Pospisil, S. Kuznetsov, M. Tatara, A. Marusic, Strouhal number of bridge cables with ice accretion at low flow turbulence, Wind and Structures 22 (2) (2016) 253–272.
[52] L. Gao, R. Veerakumar, Y. Liu, H. Hu, Quantification of the 3D shapes of the ice structures accreted on a wind turbine airfoil model, J. Vis. 22 (4) (2019) 661–667, https://doi.org/10.1007/s12650-019-00567-4.
[53] K. Zhang, H. Hu, An experimental study of the wind-driven water droplet/rivulet flows over an airfoil pertinent to wind turbine icing phenomena, Proc. ASME FEDSM 2014 (2014) 1–13, https://doi.org/10.1115/FEDSM2014-21283.
[54] K. Zhang, T. Wei, H. Hu, An experimental investigation on the surface water transport process over an airfoil by using a digital image projection technique, Exp. Fluids. 56 (2015) 173, https://doi.org/10.1007/s00348-015-2046-z.
[55] H. Veerakumar, R., Gao, L., Liu, Y., and Hu, An Experimental Study of Atmospheric Icing Process on Power Transmission Line, in: SAE Tech. Pap. 2019-01-2019, 2019. 10.4271/2019-01-2019.
[56] A.P. and J.J. Harper, Low Speed Wind Tunnel Testing, Third Edit, Wiley & Sons, 1999.
[57] J.T. Korhonen, T. Huhtamäki, O. Ikkala, R.H.A. Ras, Reliable measurement of the receding contact angle, Langmuir 29 (12) (2013) 3858–3863, https://doi.org/10.1021/la400009m.
[58] I.O. Ucar, M.D. Doganci, C.E. Cansoy, H.Y. Erbil, I. Avramova, S. Suzer, Combined XPS and contact angle studies of ethylene vinyl acetate and polyvinyl acetate blends, Appl. Surf. Sci. 257 (22) (2011) 9587–9594, https://doi.org/10.1016/j.apsusc.2011.06.070.
[59] F. Arianpour, M. Farzaneh, S.A. Kulinich, Hydrophobic and ice-retarding properties of doped silicone rubber coatings, Appl. Surf. Sci. 265 (2013) 546–552, https://doi.org/10.1016/j.apsusc.2012.11.042.
[60] A.J. Meuler, J.D. Smith, K.K. Varanasi, J.M. Mabry, G.H. McKinley, R.E. Cohen, Relationships between water wettability and ice adhesion, ACS Appl. Mater. Interfaces. 2 (11) (2010) 3100–3110, https://doi.org/10.1021/am1006035.
[61] Y. Liu, Z. Zhang, H. Hu, H. Hu, A. Samanta, Q. Wang, H. Ding, An experimental study to characterize a surface treated with a novel laser surface texturing technique: Water repellency and reduced ice adhesion, Surf. Coatings Technol. 374 (2019) 634–644, https://doi.org/10.1016/j.surfcoat.2019.06.046.
[62] E.P. Moncholi, An experimental and numerical study on the effect of some properties of non-metallic materials on the ice adhesion level, Cranfield University, 2013. http://dspace.lib.cranfield.ac.uk/handle/1826/8270 (accessed October 25, 2020).
[63] R.M. Waldman, H. Hu, High-speed imaging to quantify transient ice accretion process over an airfoil, J. Aircr. 53 (2) (2016) 369–377, https://doi.org/10.2514/1.C033367.
[64] A. Cassie, S. Baxter, Wettability of porous surfaces, accessed February 14, 2016, Trans. Faraday Soc. 40 (1944) 546–551, http://pubs.rsc.org/en/content/articlepdf/1944/tf/tf9444000546.
[65] R. Wenzel, Resistance of solid surface to wetting by water, Ind. Eng. Chem. (1936). http://pubs.acs.org/doi/pdf/10.1021/ie50320a024 (accessed September 11, 2017).
[66] M.A. Sarshar, C. Swarctz, S. Hunter, J. Simpson, C.-H. Choi, Effects of contact angle hysteresis on ice adhesion and growth on superhydrophobic surfaces under dynamic flow conditions, Colloid Polym. Sci. 291 (2) (2013) 427–435, https://doi.org/10.1007/s00396-012-2753-4.
[67] Y. Liu, H. Hu, An experimental investigation on the unsteady heat transfer process over an ice accreting airfoil surface, accessed February 24, 2018, Int. J. Heat Mass Transf. 122 (2018) 707–718, http://linkinghub.elsevier.com/retrieve/pii/S0017931017357125.
[68] M. Nosonovsky, Materials science: Slippery when wetted, Nature 477 (2011) 412–413, https://doi.org/10.1038/477412a.
[69] J. Lv, Y. Song, L. Jiang, J. Wang, Bio-inspired strategies for anti-icing, ACS Nano. (2014). http://pubs.acs.org/doi/abs/10.1021/nn406522n (accessed September 11, 2017).
[70] D. Anderson, J. Tsao, Evaluation and validation of the messinger freezing fraction, Work. Pap. (2005) 18.
[71] Y. Liu, L.J. Bond, H. Hu, Ultrasonic-attenuation-based technique for ice characterization pertinent to aircraft icing phenomena, AIAA J. (2017) 1–8, https://doi.org/10.2514/1.J055500.
[72] F. White, Viscous Fluid Flow (McGraw-Hill Mechanical Engineering), (2005) 640. http://www.amazon.com/Viscous-Fluid-McGraw-Hill-Mechanical-Engineering/dp/0072402318 (accessed September 19, 2021).
[73] J. Shin, Characteristics of surface roughness associated with leading-edge ice accretion, J. Aircr. 33 (2) (1996) 316–321, https://doi.org/10.2514/3.46940.